Isogeometric analysis of the time-dependent incompressible MHD equations

J. S. Ahn [*1] and M. J. Bluck [†1]

[1]Imperial College London, London, U.K.

February 15, 2020

Abstract

This paper presents an isogeometric (IGA) solver for time-dependent, incompressible magnetohydrodynamics (MHD). In this paper, a combination of inf-sup stable mixed discretisations is considered to discretise the hydrodynamic pair (i.e. velocity and pressure) and magnetic pair (i.e. magnetic field and magnetic pressure). The one step θ-method is used for the temporal discretisation. Manufactured and analytical solutions are considered to assess convergence, accuracy and performance of the IGA solver. Moreover, benchmark problems involving a MHD flow over an obstacle and MHD flow under non-uniform magnetic field are considered to examine the effect of the magnetic field on the flow behaviour.

Keyword

Isogeometric analysis, Incompressible, Time-dependent, Magnetohydrodynamics

[*]ja1909@ic.ac.uk
[†]m.bluck@imperial.ac.uk

1 Introduction

Magnetohydrodynamic (MHD) systems are governed by a systems of coupled equations representing the velocity/pressure fields (Navier-Stokes) and the electromagnetic fields (Maxwell's). One of the characteristics of MHD is a potentially strong force opposing the flow, known as the Lorentz force, which can have profound effects on the flow behaviour, within the core flow and in boundary layers. The boundary layers are the key features that determine pressure drop and heat transfer and for that reason, the need to represent the geometry accurately and to resolve boundary layers is pivotal in any numerical simulation of MHD flows. There are a number of studies which focus on the development of solvers for MHD flows in complex geometries. These include the use of unstructured grids [1, 2, 3] and body-fitted grids [4, 1]. In general, as with the majority of numerical methods, mesh generation (either using a body-fitted grid or an unstructured grid) for complex geometries can be costly and difficult. In [5], the potential of the isogeometric analysis solver in the application of the incompressible MHD was examined and a combination of inf-sup stable mixed discretisations was assessed. The isogeometric analysis (IGA) was introduced as a bridge between finite element analysis (FEA) and computer-aided design (CAD) [6], effectively eliminating the explicit mesh generation process. IGA employs B-splines, Non-Uniform Rational B-splines (NURBS) or T-splines, which are building blocks of geometry in the CAD to construct the domain as well as the functional spaces central to any finite element method. This has several advantages including the construction of spaces with higher regularity and increased smoothness. This has demonstrated substantially improved accuracy for problems, e.g. [6, 7, 8, 9], in comparison with conventional finite element methods. In this paper, an isogeometric analysis solver for the time-dependent, incompressible MHD problems is presented. The steady-state solver in [5] is extended to time-dependent MHD flows. In [5], a combination of inf-sup stable mixed discretisations was considered, namely TH-CURL and DIV-CURL. These were based on related studies for the Navier-Stokes problem using divergence-conforming B-splines [10, 11] and using TH B-splines [12] and Maxwell's using curl-conforming B-splines [13, 14]. TH-CURL was a combination of Taylor-Hood (TH) B-splines for Navier-Stokes equations and curl-conforming B-splines (CURL) for Maxwell's equations. Similarly, DIV-CURL was a combiation of divergence-conforming (DIV) B-splines for Navier-Stokes and CURL for Maxwell's. The main difference between the two

discretizations is that DIV-CURL produces exactly divergence-free approximations for the velocity field. Both TH-CURL and DIV-CURL are considered in this paper for comparison. We also consider the one step θ-method for the temporal discretisation using both fully-implicit and semi-implicit schemes. Solving the time-dependent MHD system can be challenging due to the coupling between the time-dependent Navier-Stokes and time-dependent Maxwell's equations. There have been several studies on the numerical solution for the time-dependent MHD system including [15, 16, 17]. From these examples, it is shown that the fully-implicit and semi-implicit schemes for the MHD system are unconditionally stable and converging. In this paper, the application of the IGA solver for time-dependent, incompressible MHD problem is to be assessed using manufactured solutions and benchmark problems. The paper is structured as follows: In section 2, for completeness, a brief introduction to the IGA, notably B-splines and NURBS, is given. In section 3, the governing equations and their variational formulation for time-dependent, incompressible MHD are presented. In section 4, spatial and time discretisations for time-dependent, incompressible MHD equations are presented. A detailed convergence study is carried out in section 5 to verify the convergence and accuracy of the solution for certain benchmark cases. Finally, a number of examples of MHD problems are considered in section 6.

2 Preliminary

A more complete description of the foundations of IGA can be found in [6, 18, 14], but the key concepts of B-splines and NURBS are introduced here for completeness and to define notation. First, a univariate B-spline is considered. A knot vector contains elements (or knots) are in an ascending order, i.e. $\xi_1 \leq \xi_2 \leq ... \leq \xi_{n+p+1}$ and is written as follows:

$$\Xi = [\xi_1, \xi_2, ...\xi_{n+p+1}] \tag{1}$$

where n is the number of basis functions and p the polynomial degree. The first knot, ξ_1 is 0 and the last knot, ξ_{n+p+1} is equal to 1. The knot vector is therefore a set of coordinates in a parametric space spanning the interval [0,1]. A knot span is defined as an interval between two unique knots and it is equivalent to an element in FE. In general, open knot vectors where the first knot and the last knot are repeated $p + 1$ times are employed, unless otherwise specified. A knot (other than the first and the last) can also be

repeated in a knot vector. In this case, this knot has the multiplicity of m and its continuity is C^{p-m} for a polynomial degree p. Let $\boldsymbol{\zeta}$ denote a vector of unique knots in Ξ. The b-spline basis functions of degree p then have $\alpha_i = p - m_i$ continuous derivatives at the knot ζ_i. The maximum multiplicity allowed in this case is $m_i = p + 1$ and at each such knot ζ_i a discontinuity is observed. Let $\boldsymbol{\alpha}$ be a vector consisting of the regularity of the knots in $\boldsymbol{\zeta}$; $\boldsymbol{\alpha} = [\alpha_1, \alpha_2, ..., \alpha_{l-1}, \alpha_l]$, with $\alpha_1 = \alpha_l = -1$ at boundaries and $\alpha_i \geq 0$ for all internal knots $2 \leq i \leq l-1$ where l is the number of unique knots. Given the knot vector, Ξ, the basis functions for univariate B-splines are calculated recursively using the Cox-de Boor recursion formula. Starting with the piecewise constant function (when $p = 0$):

$$B_i^0(\xi) = \begin{cases} 1 \ \xi_i \leq \xi \leq \xi_{i+1} \\ 0 \text{ otherwise} \end{cases} \tag{2}$$

the basis functions of degree $p \geq 1$ are defined as follows:

$$B_i^p(\xi) = \frac{\xi - \xi_i}{\xi_{i+p} - \xi_i} B_i^{p-1}(\xi) + \frac{\xi_{i+p+1} - \xi}{\xi_{i+p+1} - \xi_{i+1}} B_{i+1}^{p-1}(\xi) \tag{3}$$

Note that when $\xi_{i+p} - \xi_i$ is zero, $\frac{\xi - \xi_i}{\xi_{i+p} - \xi_i}$ is set to zero. Similarly when $\xi_{i+p+1} - \xi_{i+1}$ is zero, $\frac{\xi_{i+p+1} - \xi}{\xi_{i+p+1} - \xi_{i+1}} = 0$. The space of B-splines spanned by the univariate basis functions B_i^p is defined as follows:

$$S_{\boldsymbol{\alpha}}^p = \text{span}\{B_i^p\}_{i=1}^n \tag{4}$$

The derivatives of the functions in $S_{\boldsymbol{\alpha}}^p$ are also splines for $p \geq 1$.

$$\left\{ \frac{d}{dx} v : v \in S_{\boldsymbol{\alpha}}^p \right\} = S_{\boldsymbol{\alpha}-1}^{p-1} \tag{5}$$

The definitions for the univariate B-spline can be extended to the general multi-dimensional case using a tensor product as follows. Given integers p_j and n_j with $j = 1, ..., d$, knot vectors $\Xi_j = [\xi_{1,j}, \xi_{2,j}, ..., \xi_{n_j+p_j+1,j}]$ are introduced and vectors associated with given knot vectors are defined as $\boldsymbol{\zeta}_j = [\zeta_{1,j}, \zeta_{2,j}, ..., \zeta_{l_j,j}]$, with multiplicities $[m_{1,j}, m_{2,j}, ..., m_{l_j,j}]$ and $\boldsymbol{\alpha}_j = [\alpha_{1,j}, \alpha_{2,j}, ..., \alpha_{l_j,j}]$. The corresponding multivariate B-spline basis functions and B-spline spaces are given as follows:

$$B_{i_1,...,i_d}^{p_1,...,p_d} = B_{i_1,1}^{p_1} \otimes B_{i_2,2}^{p_2} \otimes ... \otimes B_{i_d,d}^{p_d} \tag{6}$$

where $i_j = 1, ..., n_j$ for $j = 1, ..., d$.

$$S^{p_1,...,p_d}_{\boldsymbol{\alpha}_1,...,\boldsymbol{\alpha}_d} = S^{p_1,...,p_d}_{\boldsymbol{\alpha}_1,...,\boldsymbol{\alpha}_d}(\mathcal{Q}_h) = \text{span}\{B^{p_1,...,p_d}_{i_1,...,i_d}\}^{n_1,...,n_d}_{i_1=1,...,i_d=1} \tag{7}$$

A Cartesian parametric mesh associated with these vectors which partition the parametric domain is defined as follows:

$$\mathcal{Q}_h = \{Q = \otimes_{j=1,...,d}(\zeta_{i_j,j}, \zeta_{i_j+1,j}), 1 \leq i_j \leq l_j - 1\} \tag{8}$$

For each element $Q \in \mathcal{Q}_h$, a parametric mesh of size $h_Q = \text{diam}(Q)$ can be determined. The equation (7) shows that the space is fully characterized by $\mathcal{Q}_h$, p_j and $\boldsymbol{\alpha}_j$ with $j = 1, ..., d$. The mapping of the mesh in the parametric domain to the physical domain is achieved via a B-spline/NURBS geometric mapping $\mathbf{F} : \hat{\Omega} \to \Omega$.

$$\mathbf{F} = \sum_{i=1}^{n} B^p_i(\xi)\mathbf{P}_i \tag{9}$$

where $\mathbf{P}_i$ are the control points. Note that it is assumed that the mapping $\mathbf{F}$ is invertible, with smooth inverse on each element.

3 Variational Formulation

3.1 Governing Equations

For time-dependent, incompressible MHD flow problems considered in this study, the following governing equations are considered: Given the initial velocity and magnetic field $(\mathbf{u}_0, \mathbf{b}_0)$, find $(\mathbf{u}, \mathbf{b}, p)$ such that

$$\frac{\partial \mathbf{u}}{\partial t} - \nabla \cdot (2\nu_f \nabla^s \mathbf{u}) + (\mathbf{u} \cdot \nabla)\mathbf{u} + \nabla p - \kappa(\nabla \times \mathbf{b}) \times \mathbf{b} = \mathbf{f}_u \tag{10a}$$

$$\kappa \frac{\partial \mathbf{b}}{\partial t} + \nabla \times (\nu_m \kappa \nabla \times \mathbf{b}) - \kappa \nabla \times (\mathbf{u} \times \mathbf{b}) + \nabla r = \mathbf{f}_b \tag{10b}$$

$$\nabla \cdot \mathbf{u} = 0 \tag{10c}$$

$$\nabla \cdot \mathbf{b} = 0 \tag{10d}$$

for $(\mathbf{x}, t) \in \Omega \times T$ where $\Omega \subset \mathbb{R}^d$, $d = 2, 3$. In (10), $\mathbf{u} = (u_1(\mathbf{x}, t), ..., u_d(\mathbf{x}, t))$ is the velocity field, $p = p(\mathbf{x}, t)$ the hydrodynamic pressure, $b = (b_1(\mathbf{x}, t), ..., b_d(\mathbf{x}, t))$ the magnetic field and $r = r(\mathbf{x}, t)$ the Lagrange multiplier or the magnetic

pressure. Additionally, ν_f denotes the fluid kinematic viscosity, κ denotes the coupling parameter defined as $\frac{1}{\rho_f \mu_m}$ and ν_m denotes the magnetic diffusivity defined as $\frac{1}{\mu_m \sigma_f}$, where ρ_f is the fluid density, μ_m the magnetic permeability and σ_f the electrical conductivity of the fluid. The functions on the RHS of (10) $\mathbf{f}_u$ and $\mathbf{f}_b$ are source terms for the momentum and induction equations respectively. The source in the induction equation $\mathbf{f}_b$ is solenoidal. The symmetrized gradient operator ∇^s in (10) is defined as $\nabla^s \mathbf{v} = \frac{1}{2}\left(\nabla \mathbf{v} + \nabla^T \mathbf{v}\right)$. If the kinematic viscosity ν_f is constant and $\nabla \cdot \mathbf{u} = 0$, $\nabla \cdot (2\nu_f \nabla^s \mathbf{u}) = \nu_f \Delta \mathbf{u}$. The initial conditions of the velocity and magnetic fields denoted by $\mathbf{u}_0 = \mathbf{u}(\mathbf{x}, 0)$ and $\mathbf{b}_0 = \mathbf{b}(\mathbf{x}, 0)$ respectively need to satisfy the divergence-free conditions, i.e. $\nabla \cdot \mathbf{u}_0 = 0$ and $\nabla \cdot \mathbf{b}_0 = 0$. For the boundary conditions, the domain boundary $\Gamma = \partial\Omega$ may be partitioned into two parts; one for the hydrodynamic problem denoted by the sub-script f and the other for the magnetic problem denoted by the sub-script m. The sub-scripts D and N indicate Dirichlet type and Neumann type boundary conditions respectively. In the case of the hydrodynamic problem, the following boundary conditions may be considered:

$$\begin{aligned} \mathbf{u} &= \mathbf{u}_D \quad \text{on } \Gamma_{f,D} \\ \left[-p\mathbf{I} + 2\mu_f \left(\nabla \mathbf{u} + \nabla^T \mathbf{u}\right)\right] \cdot \mathbf{n} &= \mathbf{g}_f \quad \text{on } \Gamma_{f,N} \end{aligned}$$

where $\mathbf{u}_D$ represents the velocity on the domain boundary, $\mathbf{g}_f$ the normal stress, $\mathbf{n}$ the normal vector on Γ and μ_f the fluid dynamic viscosity. Similarly, the boundary conditions for the magnetic problems can be written as follows:

$$\begin{aligned} \mathbf{n} \times \mathbf{b} = \mathbf{n} \times \mathbf{b}_D, \quad r = 0 \quad &\text{on } \Gamma_{m,D} \\ \mathbf{n} \cdot \mathbf{b} = \mathbf{n} \cdot \mathbf{b}_N, \quad \mathbf{n} \times (\nabla \times \mathbf{b}) = \mathbf{j}_\Gamma \quad &\text{on } \Gamma_{m,N} \end{aligned}$$

where $\mathbf{b}_D$ and $\mathbf{b}_N$ represent the magnetic field on the boundary and $\mathbf{j}_\Gamma$ denotes the electrical current density on the boundary; it should be noted that $\mathbf{n} \cdot \mathbf{j}_\Gamma = 0$. It is evident that (10) is over-determined without the Lagrange multiplier r due to the divergence-free constraint on the magnetic field. If the Lagrange multiplier is not included, there may be at least one solution to (10); this can be observed by applying $\nabla \cdot$ to equation (10b) from which it follows that $\frac{\partial(\nabla \cdot \mathbf{b})}{\partial t} = 0$. This implies that the divergence-free constraint on the magnetic field (10d) will always be satisfied if the initial magnetic field satisfies $\nabla \cdot \mathbf{b}_0 = 0$. However, this cannot be guaranteed for the discrete formulation of (10). For this reason, the divergence-free constraint (10d) is explicitly enforced by

introducing the Lagrange multiplier or the magnetic pressure. The system (10) can be characterised by the following non-dimensional parameters: the Reynolds number $Re = \frac{u_C l_C}{\nu_f}$, the magnetic Reynolds number $Rm = \frac{u_C l_C}{\nu_m}$, the Hartmann number $Ha = b_C l_C \sqrt{\frac{\sigma_f}{\mu_f}}$ and the coupling parameter $S = \frac{Ha^2}{ReRm}$, where u_C, b_C and l_C are the characteristic velocity, magnetic field and length respectively.

3.2 Variational Form

In order to determine the variational formulation of (10), the following functional spaces are introduced:

$$\begin{aligned}
\mathbf{V} =& \mathbf{H}_0^1(\Omega) = \{\mathbf{v} \in \mathbf{H}^1(\Omega); \mathbf{v} = 0 \text{ on } \partial\Omega\} \\
\mathbf{C} =& \mathbf{H}_0(\mathbf{curl}; \Omega) = \{\mathbf{c} \in \mathbf{L}^2(\Omega); \nabla \times \mathbf{c} \in \mathbf{L}^2(\Omega); \mathbf{n} \times \mathbf{c} = 0 \text{ on } \partial\Omega\} \\
Q =& L_0^2(\Omega) = \{q \in L^2(\Omega); \int_\Omega q d\mathbf{x} = 0 \text{ in } \Omega\} \\
S =& H_0^1(\Omega) = \{s \in H^1(\Omega); s = 0 \text{ on } \partial\Omega\}
\end{aligned}$$

They are equipped with the following norms:

$$||\mathbf{v}||_{\mathbf{V}} = \left(||\mathbf{v}||^2_{L^2(\Omega)} + ||\nabla \mathbf{v}||^2_{L^2(\Omega)}\right)^{\frac{1}{2}} \quad ||\mathbf{c}||_{\mathbf{C}} = \left(||\mathbf{c}||^2_{L^2(\Omega)} + ||\nabla \times \mathbf{c}||^2_{L^2(\Omega)}\right)^{\frac{1}{2}}$$

$$||q||_Q = ||q||_{L^2(\Omega)} \qquad ||s||_S = \left(||s||_{L^2(\Omega)} + ||\nabla s||_{L^2(\Omega)}\right)^{\frac{1}{2}}$$

The variational formulation of (10) can then be written as follows: Find $(\mathbf{u}, \mathbf{b}, p, r) \in \mathbf{V} \times \mathbf{C} \times Q \times S$ such that

$$\begin{aligned}
&\partial_t(\mathbf{u}^{n+1}, \mathbf{v}) + A_u(\mathbf{u}^{n+1}, \mathbf{v}) + N_u(\mathbf{u}^{n+1}; \mathbf{u}^{n+1}, \mathbf{v}) \\
&\quad + C_u(\mathbf{b}^{n+1}; \mathbf{v}, \mathbf{b}^{n+1}) + G_u(p^{n+1}, \mathbf{v}) = \langle \mathbf{f}_u^{n+1}, \mathbf{v} \rangle
\end{aligned} \tag{11a}$$

$$\partial_t \kappa(\mathbf{b}^{n+1}, \mathbf{c}) + A_b(\mathbf{b}^{n+1}, \mathbf{c}) + C_b(\mathbf{b}^{n+1}; \mathbf{u}^{n+1}, \mathbf{c}) + G_b(r^{n+1}, \mathbf{c}) = (\mathbf{f}_b^{n+1}, \mathbf{c}) \tag{11b}$$

$$D_u(q, \mathbf{u}^{n+1}) = 0 \tag{11c}$$

$$D_b(s, \mathbf{b}^{n+1}) = 0 \tag{11d}$$

for all $(\mathbf{v}, \mathbf{c}, q, s) \in \mathbf{V} \times \mathbf{C} \times Q \times S$ for a.e. $(0, T)$. where

$$\begin{aligned}
&A_u(\mathbf{u}, \mathbf{v}) = \textstyle\int_\Omega 2\nu_f \nabla^s \mathbf{u} : \nabla^s \mathbf{v} d\mathbf{x}; && A_b(\mathbf{b}, \mathbf{c}) = \textstyle\int_\Omega \nu_m \kappa \nabla \times \mathbf{b} \cdot \nabla \times \mathbf{c} d\mathbf{x} \\
&N_u(\mathbf{a}; \mathbf{u}, \mathbf{v}) = \textstyle\int_\Omega \frac{1}{2}(\mathbf{a} \cdot \nabla)\mathbf{u} \cdot \mathbf{v} - \frac{1}{2}(\mathbf{a} \cdot \nabla)\mathbf{v} \cdot \mathbf{u} d\mathbf{x} && \\
&C_u(\mathbf{d}; \mathbf{v}, \mathbf{b}) = -\textstyle\int_\Omega \kappa(\nabla \times \mathbf{b}) \times \mathbf{d} \cdot \mathbf{v} d\mathbf{x}; && C_b(\mathbf{d}; \mathbf{u}, \mathbf{c}) = -\textstyle\int_\Omega \kappa(\mathbf{u} \times \mathbf{d}) \cdot \nabla \times \mathbf{c} d\mathbf{x} \\
&G_u(p, \mathbf{v}) = -\textstyle\int_\Omega p \nabla \cdot \mathbf{v} d\mathbf{x}; && G_b(r, \mathbf{c}) = \textstyle\int_\Omega \nabla r \cdot \mathbf{c} d\mathbf{x} \\
&D_u(q, \mathbf{u}) = \textstyle\int_\Omega \nabla \cdot \mathbf{u} q d\mathbf{x}; && D_b(s, \mathbf{b}) = -\textstyle\int_\Omega \mathbf{b} \cdot \nabla s d\mathbf{x}
\end{aligned}$$

Note that $G_u = -D_u^T$, $G_b = -D_b^T$ and $C_u = -C_b^T$. The problem is assumed to be well-posed if the following inf-sup conditions are satisfied:

$$\inf_{q\in Q}\sup_{\mathbf{v}\in\mathbf{V}}\frac{(q,\nabla\cdot\mathbf{v})}{||q||_{L^2(\Omega)}||\mathbf{v}||_{\mathbf{H}^1(\Omega)}} \geq \beta_f > 0 \tag{12a}$$

$$\inf_{s\in S}\sup_{\mathbf{c}\in\mathbf{C}}\frac{(\nabla s,\mathbf{c})}{||s||_{H^1(\Omega)}||\mathbf{c}||_{\mathbf{H}(\mathbf{curl};\Omega)}} \geq \beta_m > 0 \tag{12b}$$

as well as the Poincaré-Friedrichs inequalities [19, 20]:

$$||\mathbf{v}||_{H^1(\Omega)} \leq C_1||\nabla\mathbf{v}|| \quad \mathbf{v}\in H^1(\Omega)^d \tag{13a}$$

$$||\mathbf{c}||_{H(\mathbf{curl};\Omega)} \leq C_2||\nabla\times\mathbf{c}|| \quad \mathbf{c}\in\mathbf{X}(\Omega) \tag{13b}$$

where $\mathbf{X}(\Omega) = \mathbf{H}(\mathbf{curl};\Omega)\cap H(\mathrm{div0};\Omega)$ and $H(\mathrm{div0};\Omega)$ is the sub-space of $H(\mathrm{div};\Omega)$ with divergence-free functions. The well-posedness of the problem (11) is proven in [21].

4 Discretisation

4.1 Spatial discretisation

For the problem in (10) to be well-posed, the inf-sup conditions (12a) and (12b) need to be satisfied both at continuous and discrete levels. One of the simplest way to satisfy this is to employ inf-sup stable elements. In this case, suitable B-spline or NURBS spaces (see Section 2) need to be employed. These discretisations for the steady MHD problems are studied in [5, 22]. For completeness, the inf-sup stable spline spaces considered in this paper are given in following sections.

4.1.1 Taylor-Hood B-splines

The Taylor-Hood B-splines, one of the inf-sup stable spaces for the hydrodynamic problem can be written as follows [23, 12]:

$$\hat{\mathbf{V}}_h^{th} = S_{\alpha_1,\alpha_2,\alpha_3}^{p_1+1,p_2+1,p_3+1}(\mathcal{Q}_h)\times S_{\alpha_1,\alpha_2,\alpha_3}^{p_1+1,p_2+1,p_3+1}(\mathcal{Q}_h)\times S_{\alpha_1,\alpha_2,\alpha_3}^{p_1+1,p_2+1,p_3+1}(\mathcal{Q}_h) \tag{14}$$

$$\hat{Q}_h^{th} = S_{\alpha_1,\alpha_2,\alpha_3}^{p_1,p_2,p_3}(\mathcal{Q}_h) \tag{15}$$

Using the standard geometrical mapping $\mathbf{F} : \hat{\Omega} \to \Omega$ in (9), the discrete spaces for velocity and pressure in the physical domain are defined as follows.

$$\mathbf{V}_h^{th} = \{\mathbf{v}_h : \mathbf{v}_h \circ \mathbf{F} \in \hat{\mathbf{V}}_{0,h}^{th}\} \tag{16}$$

$$Q_h^{th} = \{q_h : q_h \circ \mathbf{F} \in \hat{Q}_{0,h}^{th}\} \tag{17}$$

It should be noted that NURBS can be used instead of B-spline basis functions.

4.1.2 Divergence-Conforming B-splines

The divergence-conforming B-spline spaces can be constructed based on the De Rham diagram as follows [14, 10, 11]:

$$\mathbf{V}_h^{div} = S^{p_1,p_2-1,p_3-1}_{\alpha_1,\alpha_2-1,\alpha_3-1}(\mathcal{Q}_h) \times S^{p_1-1,p_2,p_3-1}_{\alpha_1-1,\alpha_2,\alpha_3-1}(\mathcal{Q}_h) \times S^{p_1-1,p_2-1,p_3}_{\alpha_1-1,\alpha_2-1,\alpha_3}(\mathcal{Q}_h) \tag{18}$$

$$Q_h^{div} = S^{p_1-1,p_2-1,p_3-1}_{\alpha_1-1,\alpha_2-1,\alpha_3-1}(\mathcal{Q}_h) \tag{19}$$

The discrete velocity and pressure spaces can be defined on the physical space using the following pull-back operators:

$$\iota_{\mathbf{u}}(\mathbf{v}) = \det(\mathrm{D}\mathbf{F})(\mathrm{D}\mathbf{F})^{-1}(\mathbf{v} \circ \mathbf{F}), \quad \forall \mathbf{v} \in H_0(\mathrm{div}, \Omega) \tag{20}$$

$$\iota_p(q) = \det(\mathrm{D}\mathbf{F})(q \circ \mathbf{F}), \quad \forall q \in L_0^2(\Omega) \tag{21}$$

The operator (20) is known as the Piola transformation. This transformation preserves the divergence-conforming property of the velocity and therefore preserves the inf-sup stability. For this velocity-pressure pair, the following statement holds:

$$\nabla \cdot \mathbf{v}_h = q_h$$

for $\mathbf{v}_h \in \mathbf{V}_h^{div}$ and $q_h \in Q_h^{div}$. This implies that the inf-sup condition for the hydrodynamic problem is satisfied.

4.1.3 Curl-Conforming B-splines

The curl-conforming B-spline spaces can be similarly constructed based on the De Rham diagram as follows [14, 13, 24]:

$$\mathbf{C}_h = S^{p_1-1,p_2,p_3}_{\alpha_1-1,\alpha_2,\alpha_3}(\mathcal{Q}_h) \times S^{p_1,p_2-1,p_3}_{\alpha_1,\alpha_2-1,\alpha_3}(\mathcal{Q}_h) \times S^{p_1,p_2,p_3-1}_{\alpha_1,\alpha_2,\alpha_3-1}(\mathcal{Q}_h) \tag{22}$$

$$S_h = S^{p_1,p_2,p_3}_{\alpha_1,\alpha_2,\alpha_3}(\mathcal{Q}_h) \tag{23}$$

The discrete magnetic pressure space can be defined on the physical space using the standard geometrical mapping defined in (9). The discrete magnetic space, on the other hand, employs the following pull-back:

$$\iota_{\mathbf{b}}(\mathbf{c}) = (\mathrm{D}\mathbf{F})^T(\mathbf{c} \circ \mathbf{F}), \quad \forall \mathbf{c} \in \mathbf{H}(\mathbf{curl}; \Omega) \tag{24}$$

In this case, the following statement is true for $\mathbf{c}_h \in \mathbf{C}_h$ and $s_h \in S_h$

$$\nabla s_h = \mathbf{c}_h$$

and therefore the inf-sup condition for the magnetic sub-problem can be satisfied.

4.2 Time discretisation

In this study, the one step θ-method is considered for the purpose of the temporal discretisation. It is assumed that the time interval $(0, T)$ is uniformly discretized into N elements. A time step size is then defined as $\delta t = \frac{T}{N}$. For the θ-discretisation, the following definitions are employed.

$$\begin{aligned} u^{n+\theta} =& \theta u^{n+1} + (1-\theta)u^n \\ \delta u^{n+1} =& u^{n+1} - u^n \\ \dot{u}^{n+1} =& \frac{\delta u^{n+1}}{\delta t} \end{aligned}$$

The problem (10) is modified as follows: Given $(\mathbf{u}^n, \mathbf{b}^n)$, find $(\mathbf{u}^{n+1}, \mathbf{b}^{n+1}, p^{n+1}, r^{n+1})$ such that

$$\dot{\mathbf{u}}^{n+1} - \nu_f \Delta \mathbf{u}^{n+\theta} + (\mathbf{a}^{n+\theta} \cdot \nabla)\mathbf{u}^{n+\theta} - \kappa(\nabla \times \mathbf{b}^{n+\theta}) \times \mathbf{d}^{n+\theta} + \nabla p^* = \mathbf{f}_u^{n+\theta} \tag{25a}$$

$$\kappa \dot{\mathbf{b}}^{n+1} + \nu_m \kappa \nabla \times (\nabla \times \mathbf{b}^{n+\theta}) - \kappa \nabla \times (\mathbf{u}^{n+\theta} \times \mathbf{d}^{n+\theta}) + \nabla r^* = \mathbf{f}_b^{n+\theta} \tag{25b}$$

$$\nabla \cdot \mathbf{u}^* = 0 \tag{25c}$$

$$\nabla \cdot \mathbf{b}^* = 0 \tag{25d}$$

for a.e. $0 \leq t \leq T$ and $\theta \in [0, 1]$. As there are no time derivatives of the pressure and the magnetic pressure, the superscript $*$ is set to $n+1$ for simplicity. If $\theta = 1$, it is a first-order scheme, and if $\theta = \frac{1}{2}$, it is a second-order scheme. There are two ways to solve the non-linear terms in (25). One

way is to solve the system via a sequence of non-linear iterations at each time step. This method is denoted as a fully-implicit (FI) scheme where we employ $\mathbf{a}^{n+\theta} = \mathbf{u}^{n+\theta}$ and $\mathbf{d}^{n+\theta} = \mathbf{b}^{n+\theta}$. Another way is to employ time extrapolations to approximate $\mathbf{u}^{n+\theta}$ and $\mathbf{b}^{n+\theta}$ in the non-linear terms. This method is denoted as a semi-implicit (SI) scheme. In case of the first order scheme (e.g. $\theta = 1$), we set $\mathbf{a}^{n+\theta}$ and $\mathbf{d}^{n+\theta}$ to $\mathbf{u}^n$ and $\mathbf{b}^n$ respectively. In case of the second order scheme ($\theta = \frac{1}{2}$), we employ $\mathbf{a}^{n+\theta} = 2\mathbf{u}^n - \mathbf{u}^{n+1}$ and $\mathbf{d}^{n+\theta} = 2\mathbf{b}^n - \mathbf{b}^{n+1}$. While the FI scheme may be more accurate than the SI scheme, it can be less efficient due to the iterations at each time step.

4.3 Discrete System

Given the spaces defined in the previous sections, the two discretisations are constructed. The first (TH-CURL) is a combination of Taylor-Hood (TH) B-spline elements and curl-conforming (CURL) B-spline elements and the second (DIV-CURL) is a combination of divergence-conforming elements (DIV) and CURL. The discrete formulation of (11) for the TH-CURL discretisation can then be written as follows: Find $(\mathbf{u}_h, \mathbf{b}_h, p_h, r_h) \in \mathbf{V}_h^{th} \times \mathbf{C}_h \times Q_h^{th} \times S_h$ such that

$$\begin{aligned} &\frac{1}{\delta t} M_{u,h}(\mathbf{u}_h^{n+1}, \mathbf{v}_h) + A_{u,h}(\mathbf{u}_h^{n+\theta}, \mathbf{v}_h) + N_{u,h}(\mathbf{a}_h^{n+\theta}; \mathbf{u}_h^{n+\theta}, \mathbf{v}_h) \\ &+ C_{u,h}(\mathbf{b}_h^{n+\theta}; \mathbf{v}_h, \mathbf{d}_h^{n+\theta}) + G_{u,h}(p_h^{n+1}, \mathbf{v}_h) = \\ &\langle \mathbf{f}_u^{n+\theta}, \mathbf{v}_h \rangle + \frac{1}{\delta t} M_{u,h}(\mathbf{u}_h^n, \mathbf{v}_h) \end{aligned} \tag{26a}$$

$$\begin{aligned} &\frac{\kappa}{\delta t} M_{b,h}(\mathbf{b}_h^{n+1}, \mathbf{c}_h) + A_{b,h}(\mathbf{b}_h^{n+\theta}, \mathbf{c}_h) \\ &+ C_{b,h}(\mathbf{d}_h^{n+\theta}; \mathbf{u}_h^{n+\theta}, \mathbf{c}_h) + G_{b,h}(r_h^{n+1}, \mathbf{c}_h) = \\ &(\mathbf{f}_b^{n+\theta}, \mathbf{c}_h) + \frac{\kappa}{\delta t} M_{b,h}(\mathbf{b}_h^n, \mathbf{c}_h) \end{aligned} \tag{26b}$$

$$D_{u,h}(q_h, \mathbf{u}_h^{n+1}) = 0 \tag{26c}$$

$$D_{b,h}(s_h, \mathbf{b}_h^{n+1}) = 0 \tag{26d}$$

for all $(\mathbf{v}_h, \mathbf{c}_h, q_h, s_h) \in \mathbf{V}_h^{th} \times \mathbf{C}_h \times Q_h^{th} \times S_h$. where

$$
\begin{aligned}
&M_{u,h}(\mathbf{u}_h, \mathbf{v}_h) = \textstyle\int_\Omega \mathbf{u}_h \cdot \mathbf{v}_h d\mathbf{x} \\
&M_{b,h}(\mathbf{b}_h, \mathbf{c}_h) = \textstyle\int_\Omega \mathbf{b}_h \cdot \mathbf{c}_h d\mathbf{x} \\
&A_{u,h}(\mathbf{u}_h, \mathbf{v}_h) = \textstyle\int_\Omega 2\nu_f \nabla^s \mathbf{u}_h : \nabla^s \mathbf{v}_h d\mathbf{x} \\
&A_{b,h}(\mathbf{b}_h, \mathbf{c}_h) = \textstyle\int_\Omega \nu_m \kappa \nabla \times \mathbf{b}_h \cdot \nabla \times \mathbf{c}_h d\mathbf{x} \\
&N_{u,h}(\mathbf{a}_h; \mathbf{u}_h, \mathbf{v}_h) = \textstyle\int_\Omega \frac{1}{2}(\mathbf{a}_h \cdot \nabla)\mathbf{u}_h \cdot \mathbf{v}_h - \frac{1}{2}(\mathbf{a}_h \cdot \nabla)\mathbf{v}_h \cdot \mathbf{u}_h d\mathbf{x} \\
&C_{u,h}(\mathbf{d}_h; \mathbf{v}_h, \mathbf{b}_h) = -\textstyle\int_\Omega \kappa(\nabla \times \mathbf{b}) \times \mathbf{d}_h \cdot \mathbf{v}_h d\mathbf{x} \\
&C_{b,h}(\mathbf{d}_h; \mathbf{u}_h, \mathbf{c}_h) = -\textstyle\int_\Omega \kappa(\mathbf{u}_h \times \mathbf{d}_h) \cdot \nabla \times \mathbf{c}_h d\mathbf{x} \\
&G_{u,h}(p_h, \mathbf{v}_h) = -\textstyle\int_\Omega p_h \nabla \cdot \mathbf{v}_h d\mathbf{x}; \\
&G_{b,h}(r_h, \mathbf{c}_h) = \textstyle\int_\Omega \nabla r_h \cdot \mathbf{c}_h d\mathbf{x} \\
&D_{u,h}(q_h, \mathbf{u}_h) = \textstyle\int_\Omega \nabla \cdot \mathbf{u}_h q_h d\mathbf{x}; \\
&D_{b,h}(s_h, \mathbf{b}_h) = -\textstyle\int_\Omega \mathbf{b}_h \cdot \nabla s_h d\mathbf{x}
\end{aligned}
$$

The discrete formulation based on the DIV-CURL discretisation is similar, except that the terms $A_{u,h}$ and $N_{u,h}$ are modified, as the tangential Dirichlet boundary conditions are not satisfied in the divergence-conforming spaces. For that reason, the Nitsche's method is used to weakly enforce the Dirichlet conditions [18, 25]. The bilinear term $A_{u,h}$ is accordingly modified as follows: For $\mathbf{u}_h, \mathbf{v}_h \in \mathbf{V}_h^{div}$.

$$
\begin{aligned}
A_{u,h}^{div}(\mathbf{u}_h, \mathbf{v}_h) = A_{u,h}(\mathbf{u}_h, \mathbf{v}_h) - \\
\sum_{F \in \Gamma_h} \int_F 2\nu_f \left(((\nabla^s \mathbf{v}_h)\,\mathbf{n}) \cdot \mathbf{u}_h + ((\nabla^s \mathbf{u}_h)\,\mathbf{n}) \cdot \mathbf{v}_h - \frac{C_p}{h_F} \mathbf{u}_h \cdot \mathbf{v}_h \right) d\mathbf{s}
\end{aligned} \tag{27}
$$

where C_p is a positive penalty constant, p the polynomial degree of the velocity space and h_F the mesh size at a boundary. Additionally, as the divergence-conforming velocity is considered, there is no need to use the skew-symmetric representation for the convection term:

$$
N_{u,h}^{div}(\mathbf{a}_h; \mathbf{u}_h, \mathbf{v}_h) = \int_\Omega (\mathbf{a}_h \cdot \nabla)\mathbf{u}_h \cdot \mathbf{v}_h d\mathbf{x} \tag{28}
$$

5 Convergence Analysis

In this section, some benchmark results of the isogeometric analysis are presented. The results are validated against analytical solutions and manufactured solutions, allowing a detailed study of the convergence and stability of

the method. In some cases, a comparison is made with conventional FE where available. When the fully-implicit scheme is used, the tolerance (defined as the ratio of current residual to the initial residual) is set to 1.0^{-4} for the non-linear iterations. The L^2 norms of errors defined as $||e|| = ||u - u_h||_{L^2(\Omega)}$, where u is the manufactured (or analytical) solution and u_h is the numerical solution are determined to assess the convergence of solutions. In this paper, a direct solver (MUMPS) has been employed to demonstrate the capability of the proposed method. This however may not result in an optimised performance of the proposed solver. In order to reduce the computational cost for larger problems, it may be necessary to build a problem-specific preconditioner [26, 27, 28].

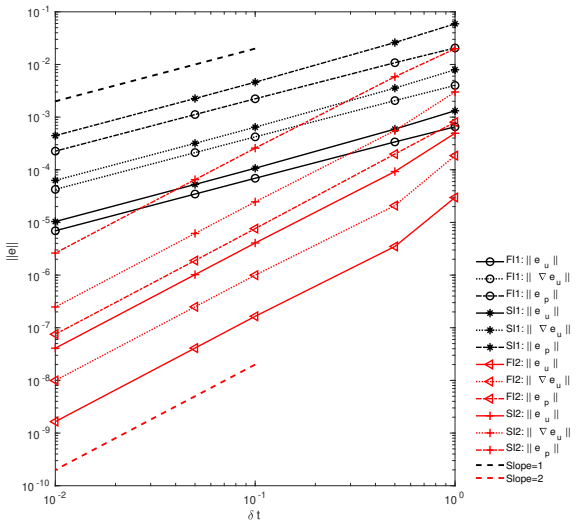
5.1 Example 1: Manufactured Solution

In this example, different time discretisations are employed to compare the accuracy and convergence rates of a number of schemes: fully-implicit 1st order (FI1) scheme, fully-implicit 2nd order (FI2) scheme, semi-implicit 1st order (SI1) scheme and semi-implicit 2nd order (SI2) scheme. In this example, a two-dimensional domain $\Omega = (0,1)^2$ with $\Gamma_N = \{(1,y) : y \in (0,1)\}$ and $\Gamma_D = \partial\Omega \setminus \Gamma_N$ is considered. The time interval of this example is $t \in [0, t_{end}]$, where t_{end}=10.0. The source terms and inhomogeneous boundary conditions are determined such that the solution for this example is given as follows:

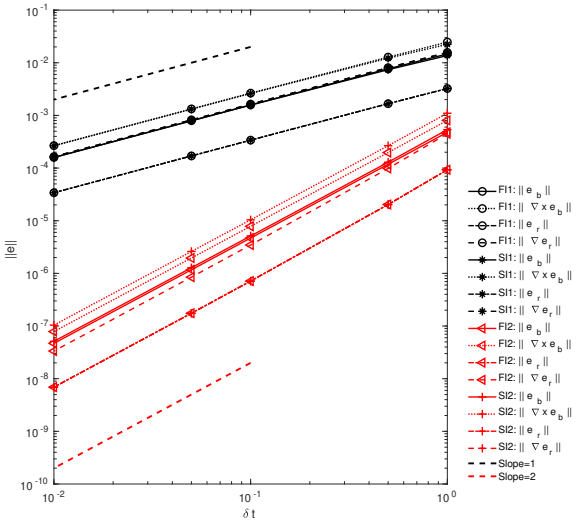
$$
\begin{aligned}
\mathbf{u}(x,y,t) &= \begin{bmatrix} y\sin(\frac{\pi t}{10})\exp(\frac{x}{25}) \\ -x\sin(\frac{\pi t}{10})\exp(\frac{x}{25}) \end{bmatrix} \\
\mathbf{b}(x,y,t) &= \begin{bmatrix} y\sin(\frac{\pi t}{10})\exp(\frac{x}{25}) \\ -x\sin(\frac{\pi t}{10})\exp(\frac{x}{25}) \end{bmatrix} \\
p(x,y,t) &= x + y \\
r(x,y,t) &= 0
\end{aligned}
$$

The fluid properties, ν_f, ν_m and κ are all set to 1.0. In this example, the error norms are computed at the end time, e.g. $||e_u|| = ||u(t = t_{end}) - u_h(t = t_{end})||_{L^2(\Omega)}$. In order to examine the convergence with respect to the time step size δt, the mesh size is fixed at 2^{-4} and only the DIV-CURL mesh scheme is considered (TH-CURL results are identical in this context). Figure 1 shows the convergence rates with respect to different time discretisation schemes. It is evident that for all schemes, the rate of convergence is optimal. In general, the second order scheme obtains a smaller error than the first order

scheme for a given time step size, as would be expected. Notably, in Figure 1a, the differences between the FI and SI schemes are more noticeable in the hydrodynamic solutions, for the second order scheme. In this case, for a velocity error of 10^{-6}, the time step size required is approximately 0.2 and 0.05 for the FI and SI schemes respectively. The differences between the FI and SI schemes are almost negligible for the magnetic solutions. Figure 2



(a) Convergence of hydrodynamic solutions at $t = t_{end}$



(b) Convergence of magnetic solutions at $t = t_{end}$

Figure 1: Convergence analysis of example 1

shows the computational time taken to reach the end time of a simulation. For a given time step size, the difference between the first and second order schemes (semi- or fully-implicit) is almost negligible - however the solution for the second order scheme will be more accurate. In short, there is negligible computational overhead as a result of the use of a second order scheme for a given step size. However, for a given time step size, the fully-implicit schemes require more than twice the time required by the corresponding semi-implicit schemes. These results suggest that a second-order semi-implicit scheme is

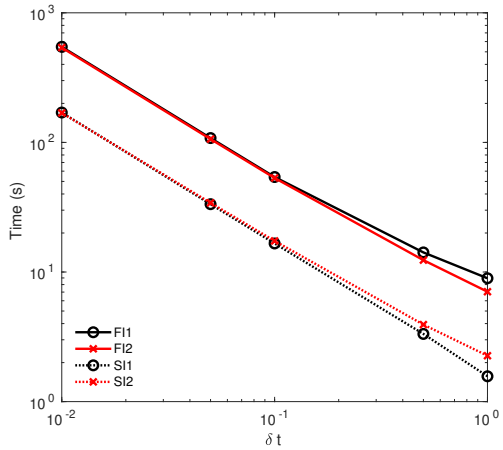


Figure 2: Computational time for example 1

likely to be the most effective in terms of cost vs. accuracy.

5.2 Example 2: Dissipative System

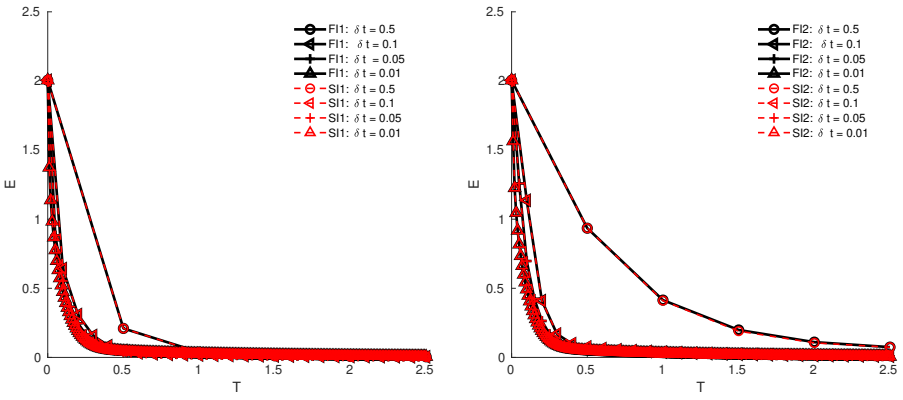
In this section, a dissipative MHD system is considered to examine the stability of the solver. Here, a two-dimensional domain $\Omega = (0,1)^2$ with $\Gamma_D = \partial\Omega$ is considered. The source terms are set to zero. The fluid properties are assumed to be constant and uniform; $\nu_f = 0.01$, $\nu_m = 1$ and $\kappa = 10$. The initial conditions of the velocity and magnetic field are given as follows:

$$\mathbf{u}_0 = \begin{bmatrix} y^2(1-y) \\ x^2(1-x) \end{bmatrix}$$

$$\mathbf{b}_0 = \begin{bmatrix} y^2 \\ (1-x^2) \end{bmatrix}$$

The system energy which is defined as $E = \left(||\mathbf{u}(t)||^2_{L^2(\Omega)} + \kappa ||\mathbf{b}(t)||^2_{L^2(\Omega)} \right)^{\frac{1}{2}}$ is recorded at each time step and the evolution of E is shown in Figures 3 and 4. Four different time step sizes are considered for comparison; $\delta t = 0.5$, 0.1, 0.05 and 0.01. Figures 3 and 4 show the evolution of the system energy for the TH-CURL and DIV-CURL schemes respectively. It shows that the rate of dissipation in the system energy increases with decreasing time-step size. In general, the first order schemes dissipate faster than the second order schemes. It also shows that there is a negligible difference between the system energy obtained using different time discretisation schemes for a given order. This suggest that the solver may be unconditionally stable.

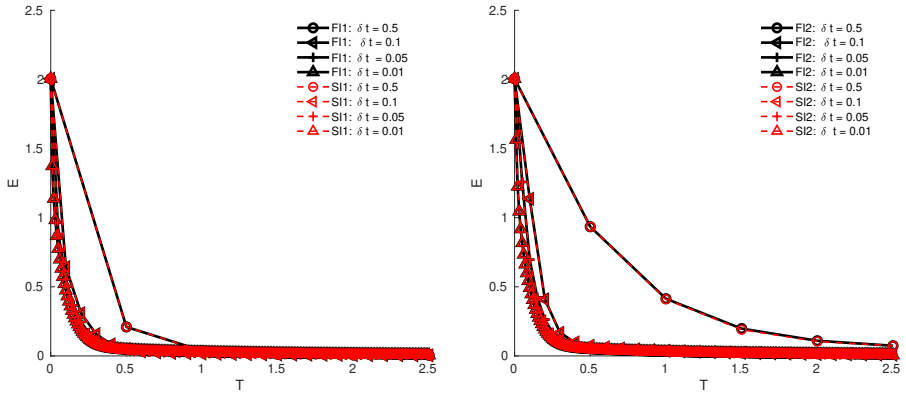
Figure 5 shows the computational time spent to reach the end time of a



(a) First order schemes (b) Second order schemes

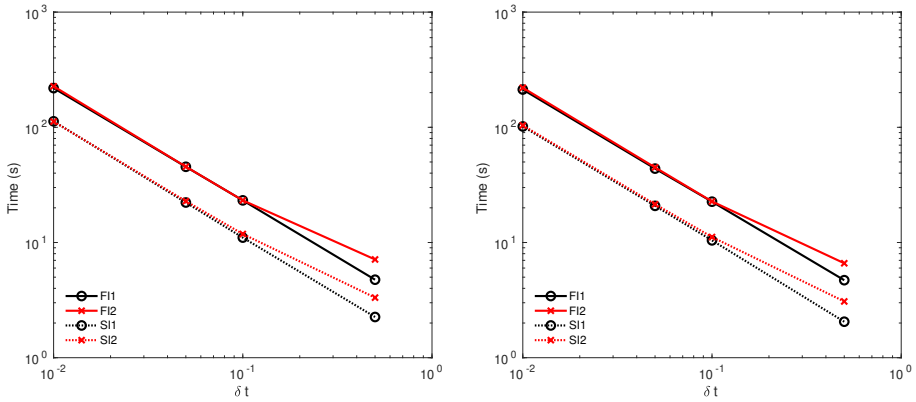
Figure 3: Evolution of the system energy obtained using TH-CURL scheme

simulation. In this case, it demonstrates that the SI schemes require less than half the time required for the FI schemes to reach the end state. For the time step size $\delta t \leq 0.1$, the difference between the first order and second order schemes appear negligible. The example 1 and example 2 show that the SI schemes generally require less than half the time required by the FI schemes to reach the end state for a given time step size. The difference in the computational cost is almost negligible between the first and second order schemes. However, the second order schemes in general achieve higher accuracy for a given time step size. While the accuracy in the magnetic solutions seems unaffected by different implicit schemes, the accuracy in the hydrodynamic solutions deteriorates, if a semi-implicit scheme is employed for a given time step size. However, it appears that the computational time



(a) First order schemes (b) Second order schemes

Figure 4: Evolution of the system energy obtained using DIV-CURL scheme



(a) DIV-CURL (b) TH-CURL

Figure 5: Computational time of example 2

of the FI and SI schemes for a given error in the velocity solution appears to be comparable. The FI schemes, however, involve solving a linear system multiple times per time step, thereby increasing the numerical work. For that reason, the second-order SI scheme is used in the following sections.

5.3 Example 3: Shercliff's Case

In this example, we consider Shercliff's case [29], which is a canonical MHD problem, and focus on the effect of spatial discretisation. In this problem, a steady-state, incompressible, laminar and fully-developed MHD flow in a

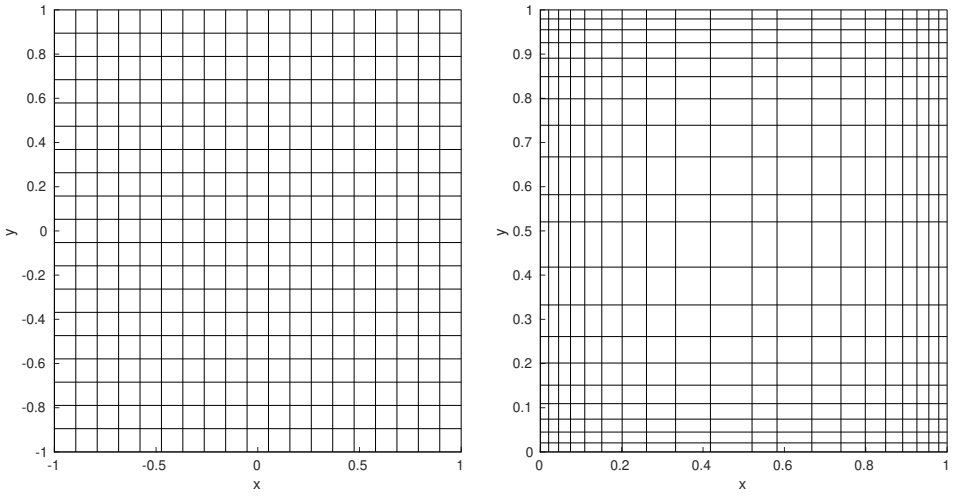
rectangular duct is considered and the equations are solved until a steady state is reached. A relatively large time step size of $\delta t = 10.0$ is considered, as it is a steady-state problem and the time interval of the simulation is $t \in [0, 50\delta t]$. For this example, the computational domain is considered to be a slice of a rectangular duct. A periodic boundary condition is then prescribed at both inlet and outlet to enforce fully-developed flow conditions. Moreover, to enforce fully-developed conditions, the external body force $\mathbf{f}_u$ is set to the following pressure gradient:

$$\frac{dp}{dz} = \frac{K l_c^3}{\rho_f \nu_f^2 Re}$$

where $K = \frac{Ha}{1-0.825Ha^{-0.5}-Ha^{-1}}$ [30]. The source term in (10b) $\mathbf{f}_b$ is set to 0. The external applied magnetic field denoted by b_C is assumed to be uniform and constant. The fluid properties ν_f, ν_m and κ are set to 1, 1 and 1 respectively. Two values of the Hartmann number are considered for this example: $Ha =$ 10 and 100. In the rectangular duct, there are two quantitatively different behaviours at walls. Two are called Hartmann walls which are perpendicular to the external magnetic field, and the other two are called side which are parallel to the external magnetic field. In Shercliff's case, both the Hartmann and side walls are insulating. The boundary conditions for Shercliff's case can then be prescribed as follows. No-slip condition is applied at walls for velocity, i.e. $\mathbf{u} = \mathbf{u}_D = \mathbf{0}$. At insulating walls, the following Dirichlet type boundary condition is applied for the magnetic problem.

$$\mathbf{n} \times \mathbf{b} = \mathbf{n} \times \mathbf{b}_D$$
$$r = 0$$

where $\mathbf{n}$ is the outward pointing unit normal vector and $\mathbf{b}_D = (0, b_0)$, where $b_0 = 10$ and 100 for $Ha = 10$ and 100 respectively. One characteristic of MHD flow in a duct is that the thickness of the boundary layers depends on the Hartmann number. In Shercliff's case, the thickness of the boundary layer at a Hartmann wall (Hartmann layer) scales as $O(Ha^{-1})$, while the thickness of the boundary layer at a side wall (side layer) scales as $O(Ha^{-\frac{1}{2}})$. This means that a very fine boundary layer is observed at higher Hartmann number. In order to resolve this without excessive mesh discretisation, a graded mesh (see Figure 6b) can be employed. For that reason, the non-uniform mesh is employed for the case with $Ha = 100$, while the uniform mesh (see Figure 6a)

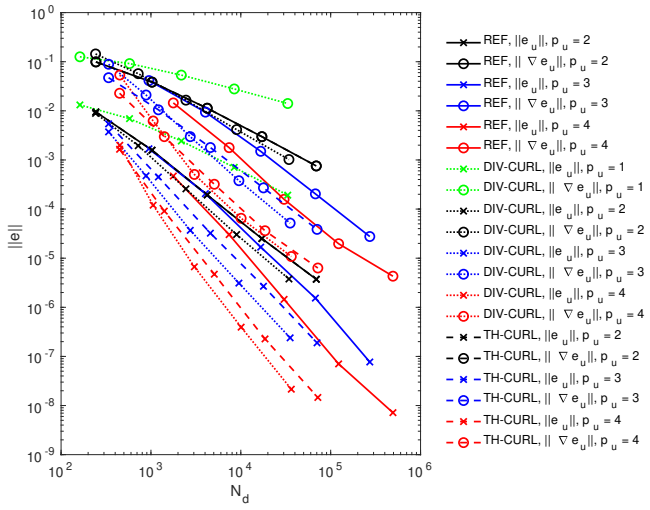


(a) Uniform mesh (b) Non-uniform mesh

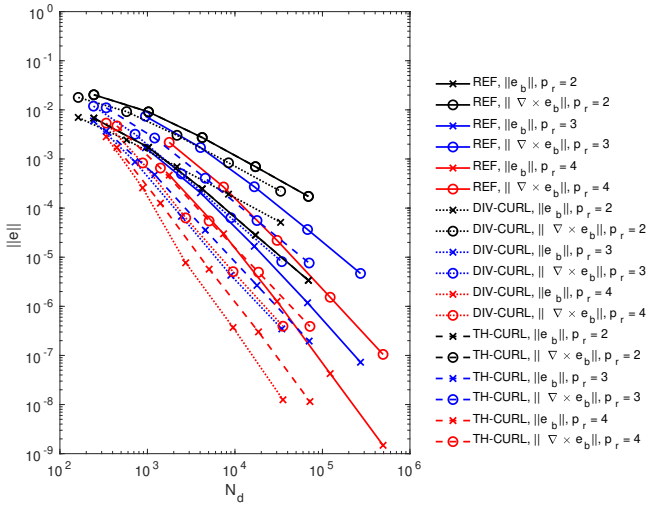
Figure 6: Mesh configuration for Shercliff's problem

is employed for the case with $Ha = 10$. In this example, a reference solution obtained using the TH-CURL scheme with C^0-continuity across the element boundary is included for comparison. This can be assumed to be equivalent to a conventional finite element solver. Figure 7 shows the convergence of both hydrodynamic and magnetic solutions for the case with $Ha = 10$ with respect to the number of unknowns (N_d). In the case with $Ha = 10$, a uniform mesh configuration is used. This shows the L^2 error in the hydrodynamic and magnetic solutions and their spatial derivatives. It is evident that lower errors and a higher convergence rate in the hydrodynamic solutions are produced, as the polynomial degree of the velocity space, p_u increases. The differences between the spatial discretisation schemes are also demonstrated in Figure 7, which includes the the reference solution (denoted by 'REF') obtained using the TH-CURL discretisation with C^0-continuity across the element boundaries. Figure 7a shows that for a given p_u and error, a smaller N_d is required by the DIV-CURL scheme. For instance, for $p_u = 4$ and $||e_u||$ = 1.0E-6, the DIV-CURL scheme requires approximately 5.0E3 unknowns, while the TH-CURL and the REF require approximately 1.0E4 and 4.0E4 unknowns respectively. This demonstrates that the DIV-CURL scheme can reduce the computational cost as well as produce divergence-free velocity solutions. Figure 7b similarly demonstrates the advantage of the DIV-CURL scheme, as lower N_d is needed for a given polynomial degree of the magnetic

pressure space, p_r and error. The case with $Ha = 10$ is also used to present



(a) Hydrodynamic solutions

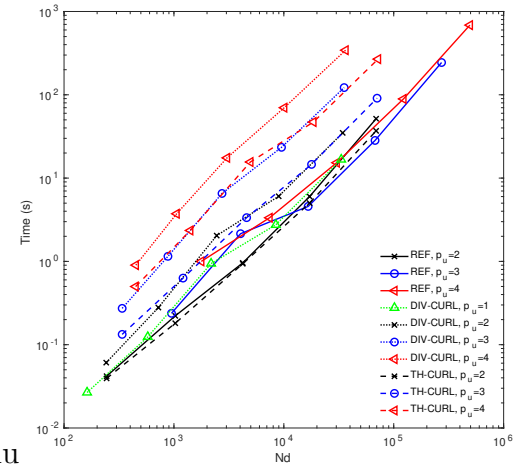


(b) Magnetic solutions

Figure 7: Convergence of solutions at $Ha = 10$

the computational cost. For some schemes, the computational time is extrapolated, as the error is outside the limits considered in Figure 7. Figure 8 shows the computational cost per step for all the schemes. It is important to consider the performance of the IGA scheme. The principal cost is the matrix solution using the solver MUMPS [31], which has been used previously

in IGA. As stated in [31], the MUMPS algorithm has a serial performance in 2D of $O(N^{1.5}p^3)$ and in 3D of $O(N^2p^3)$. This means that for the same number of degrees of freedom, high order (p) IGA is very much more expensive than low order or the REF case. This is confirmed in the timings shown in Figure 8. However, as indicated earlier, such a comparison is misleading. As discussed above, Figure 7 shows that the number of degrees of freedom needed for a given error are much lower for high order IGA. Indeed, in any given case, it is the error that determines our discretization requirements. In order to compare the performance of different schemes, we consider the cost for a given error. If we fix the error ($||e_u||$=1.0E-6), then we can estimate the degrees of freedom required (from Figure 7) and consequently the cost (Figure 8). Table 1 presents the computational cost per step for each scheme.



blu

Figure 8: Computational cost

The advantage of high order (irrespective of scheme) is clear, however, it is not self-evident that the high order continuity of IGA is of practical benefit in this case. That said, it would be unwise to conclude this generally. The Shercliff case does not take advantage of the ability of IGA to accurately model more complex geometries, where there may be considerable performance benefits. Parallelization is also a potential route to increasing the performance. MUMPS can be applied to multicore/multiprocessor systems and, with sufficient cores, exhibits performance in 2D of $O(Np^2)$ and in 3D of $O(N^{4/3}p^2)$ [31]. This reduced scaling can further improve the computational efficiency of IGA, but requires a detailed study considering the dependence

on platform and implementation, and is outside of the scope of the present work. Figure 9 shows the convergence of both hydrodynamic and magnetic

Table 1: Computational cost for $||e_u||$=1.0E-6

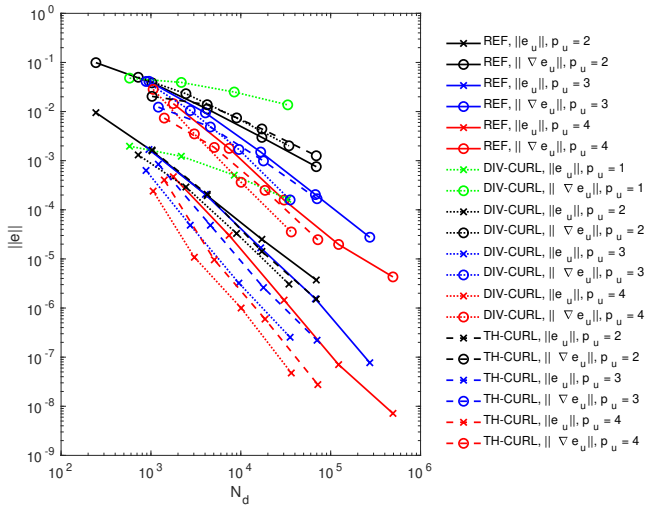
Scheme	Nd	Time (s)
REF, p_u=2	1.8E5	2.3E2
REF, p_u=3	8.3E4	3.9E1
REF, p_u=4	3.6E4	1.9E1
TH-CURL, p_u=2	1.8E5	1.5E2
TH-CURL, p_u=3	2.8E4	2.9E1
TH-CURL, p_u=4	9.9E3	2.7E1
DIV-CURL, p_u=2	8.0E4	1.3E2
DIV-CURL, p_u=3	1.7E4	4.8E1
DIV-CURL, p_u=4	6.8E3	4.4E1

solutions for the case with $Ha = 100$ with respect to N_d. In the case with $Ha = 100$, a non-uniform mesh configuration is employed. Similar to the case with $Ha = 10$, Figure 9 demonstrates that for a given error and appropriate polynomial degree, the DIV-CURL requires a smaller number of unknowns, in comparison with the TH-CURL scheme. From this example, it is found that a large reduction in number of unknowns can be achieved by the DIV-CURL scheme and a higher-order scheme. Further improvement in the performance of the solver through different routes such as optimised algorithm and parallelization could be considered as future work. However, in the following sections where more complex geometries are considered, the DIV-CURL scheme is to be used, as well as the second-order semi-implicit time stepping scheme.

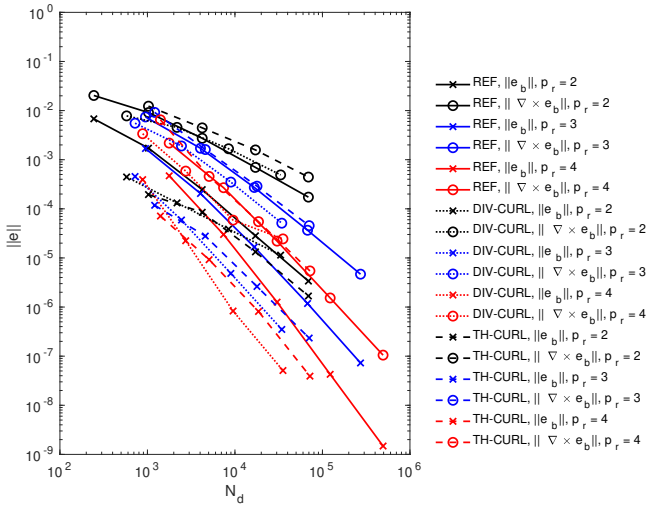
6 Results

6.1 Benchmark Case 1

In the following sections, some benchmark problems are considered. In particular, flow past an obstacle is considered. In the case of a hydrodynamic flow, the obstacle can induce turbulence even at low to intermediate Reynolds number, i.e. $Re \sim O(10^1) - O(10^2)$. Within this range of Reynolds numbers, the hydrodynamic flow starts to become unstable and vortices shed from the



(a) Hydrodynamic solutions



(b) Magnetic solutions

Figure 9: Convergence of solutions at $Ha = 100$

obstacle. This behaviour continues to the downstream and a periodic solution is observed [32]. It is however known that the effects of turbulence can be suppressed when a magnetic field is applied to the system in (10) [33], thereby eliminating the transient response and the periodic solution. This example is therefore employed to demonstrate the effect of the magnetic field on the flow over an obstacle and assess the capability of the proposed solver.

The computational domains considered for this example are shown in Figures 10 and 16. Both square and circular obstacles are considered. The characteristic length of an obstacle is denoted by D, while the height and length of the overall domain are denoted by H and L respectively. The values of H and L are sufficiently large so that they do not affect the solution past the obstacle [32]. In this example, the dimensions are set such that $D = 1$, $H = 31$ and $L = 62$. For the transient response, the Strouhal (St) number is determined as follows:

$$St = \frac{fD}{u_m}$$

where f is the frequency of the vortex shedding and u_m the mean velocity. The time interval of these examples is set to $t \in [0.0, 300.0]$. In case of low Hartmann cases ($Ha \sim O(1)$), where the effect of magnetic field is minimal, the Strouhal number is to be evaluated and compared to the experimental and numerical results involving a conventionally hydrodynamic flow [34, 35, 36, 37, 38]. In the case of the circular obstacle, the Strouhal number is compared to the result obtained from a finite element solver [39], which solved a problem involving MHD flow over a circular obstacle. For these examples, the second order semi-implicit DIV-CURL scheme with $p_p = 2$ is employed. The computational domains in Figures 10 and 16 are generated via the multiple patch configuration. Additionally, a graded mesh is employed near the obstacle. The boundary conditions for the hydrodynamic problem are prescribed as follows. At the inlet (the L.H.S. of the domain), an inlet velocity $\mathbf{u}_{in} = (1, 0)$ is prescribed. At the outlet (the R.H.S. of the domain), the zero Neumann boundary conditions are applied. At the lower, upper boundaries and the obstacle, the no-slip boundary conditions are applied. On the other hand, for the magnetic problem, the Dirichlet type boundary conditions i.e. $\mathbf{b} \times \mathbf{n} = \mathbf{b}_D \times \mathbf{n}$ and $r = 0$ where $\mathbf{b}_D = (0, b_C)$ are applied at every boundary and $b_C = Ha$ in this example. The fluid properties are assumed to be uniform and constant; $\nu_f = 0.01$, $\nu_m = 1$ and $\kappa = 1$. This sets the Reynolds number (Re) to 100. In order to evaluate the effect of the magnetic field on the flow behaviour, the following Hartmann numbers are considered: $Ha = 1$, 5 and 10. In case of $Ha = 1$, the mesh convergence study is carried out to determine the optimal number of degrees of freedom. The case with a square obstacle is used as an example to present the divergence of the magnetic field and the computational cost.

6.1.1 Flow over Square Obstacle

The computational domain for the example with the square obstacle is shown in Figure 10. Figure 11 shows the convergence of the Strouhal number with

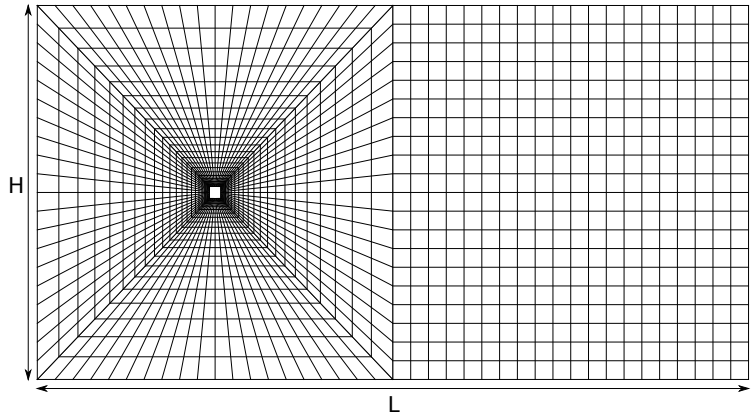


Figure 10: Mesh configuration for the domain with square obstacle

respect to the number of unknowns (N_d) for the case with $Ha = 1$. The minimum number of unknowns required to solve this example is determined to be approximately 2×10^4. The numerical results presented in this section are obtained using the most fine mesh. The Strouhal number obtained for the example with the square obstacle is approximatley 0.139. This value is similar to those obtained in [34, 35], i.e. ~ 0.138. In the following section, the solutions of this example are presented. Figure 12 shows the divergence of the magnetic field with respect to the number of unknowns. The divergence of the magnetic field decreases with increasing number of unknowns. The rate of reduction is proportional to $N_d^{-0.5}$. Figure 13 shows the computational cost of this example with respect to the number of unknowns. On the left axis, it shows the time taken to solve a single time step, while on the right axis it shows the time taken to solve a transient problem. Figure 14 shows the effect of the magnetic field on the velocity distribution at t=200.0. In case of $Ha = 1$, the periodic behavior of the velocity past the obstacle is noticeable. However, this behavior is eliminated, as the Hartmann number and therefore the magnetic field increases. When $Ha = 5$, the periodic solu-

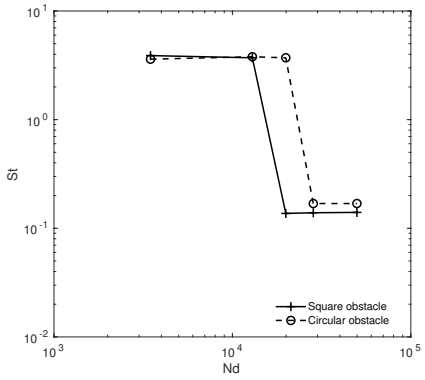


Figure 11: Mesh convergence study for flow over obstacle

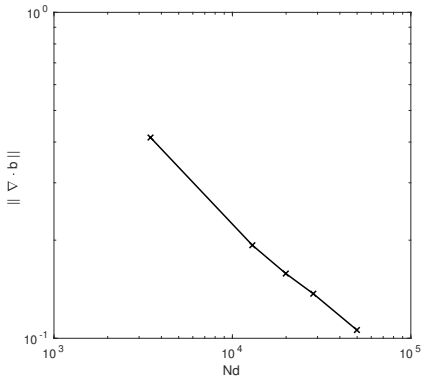


Figure 12: Divergence of magnetic field

tions are completely eliminated. Figure 15 shows the effect of the magnetic field on the pressure distribution in the domain at t=200.0. Similar to the velocity distribution, the pressure exhibits a periodic behavior at $Ha = 1$ past the obstacle and this behavior is removed as the Ha increases. Moreover, it shows that as Ha increases, the pressure drop across the obstacle increases.

6.1.2 Flow over Circular Obstacle

The computational domain and the mesh configuration of this example are shown in Figure 16. Similar to the example with the square obstacle, the mesh convergence study is carried out to determine the minimum number of unknowns required to solve this example (see Figure 11). In this case, the minimum N_d required for this example is approximately 3×10^4. The results

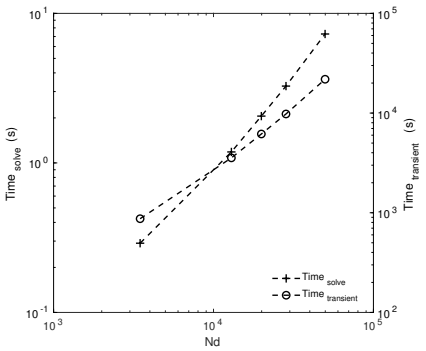
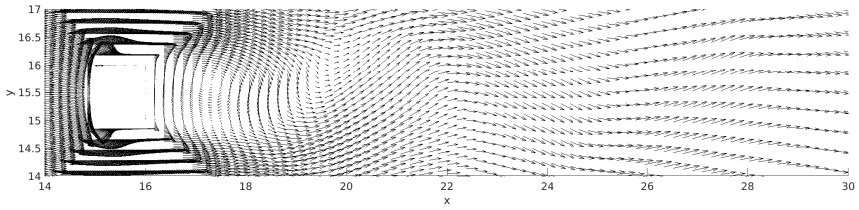
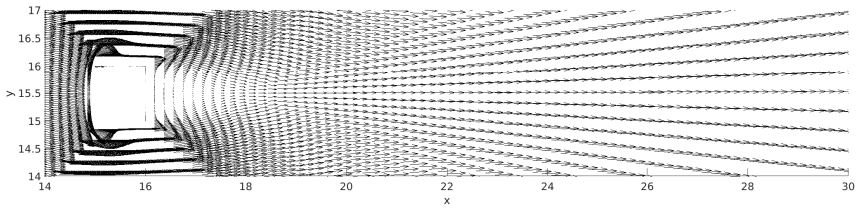


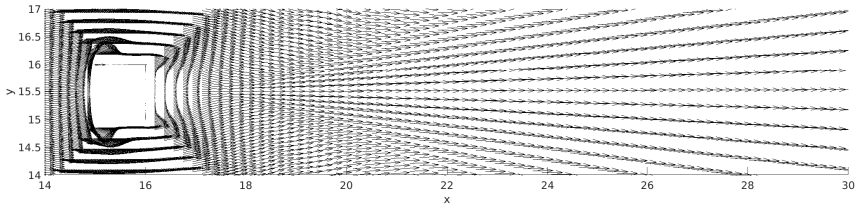
Figure 13: Computational cost



(a) $Ha = 1$



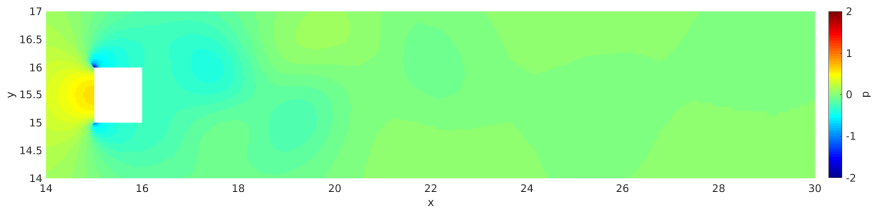
(b) $Ha = 5$



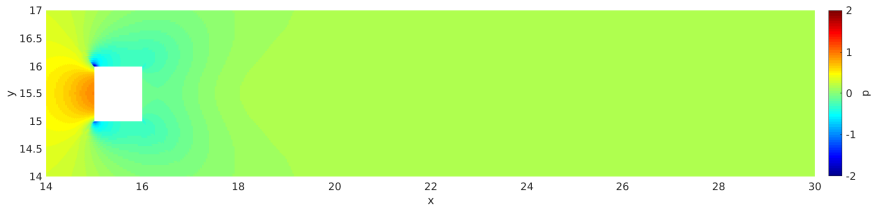
(c) $Ha = 10$

Figure 14: Velocity vector plot for flow over the square obstacle in the region $(14, 14) \times (30, 17)$

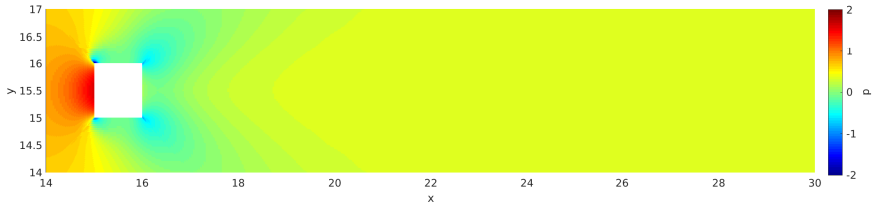
presented in this section are based on the most fine mesh. The Strouhal number (St) determined for this example with $Ha = 1$ is approximately



(a) $Ha = 1$



(b) $Ha = 5$



(c) $Ha = 10$

Figure 15: Pressure distribution for flow over the square obstacle in the region $(14, 14) \times (30, 17)$

0.169. This value is compared to that obtained in [39] which investigated the stability and long-term dissipativity of the time integration algorithms for the incompressible MHD problems. The study in [39] found that St was approximately 0.167 for $Ha = 0$ and 1. For the hydrodynamic cases, similar values for St are obtained in the other works, where St varies between 0.166 and 0.172 [36, 37, 38]. Figure 17 shows the effect of the magnetic field on the velocity distribution in the domain with a circular obstacle at t=200.0. Similar to the square obstacle, a periodic behaviour is observed at $Ha = 1$. This behaviour is removed, as the Hartmann number, and therefore the magnetic field, increase. Figure 18 shows the effect of the magnetic field on the pressure distribution in the domain with a circular obstacle. Again, a periodic behavior is observed at $Ha = 1$. As the Ha increases, the periodic behavior is removed and the pressure drop across the obstacle increases.

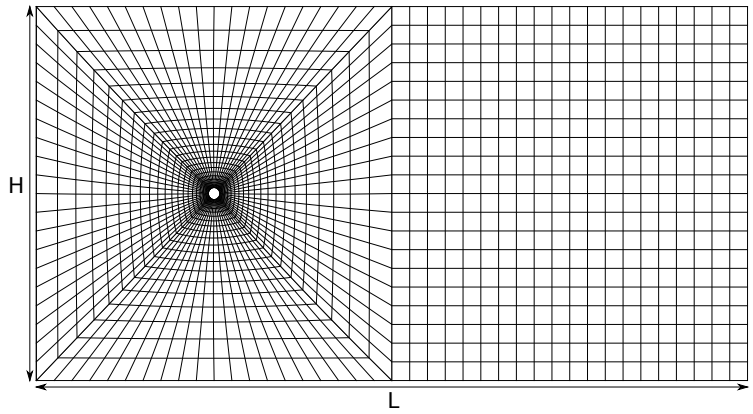


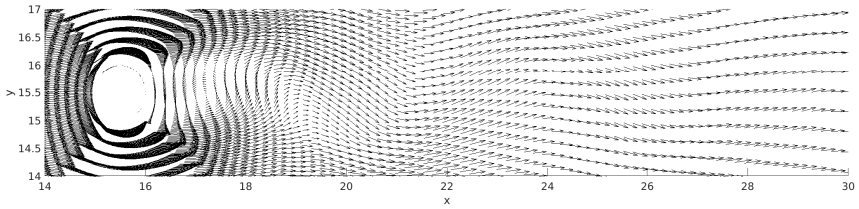
Figure 16: Mesh configuration for the domain with circular obstacle

6.2 Benchmark Case 2

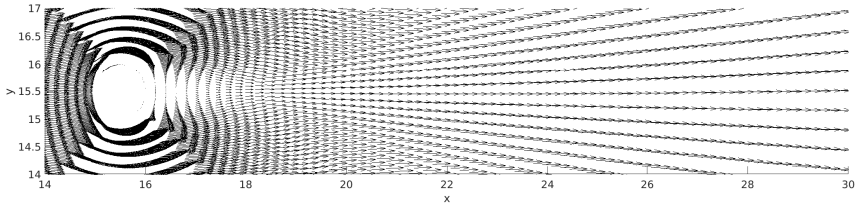
The following section considers the effect on non-uniform magnetic field on liquid metal flow in a duct. Liquid metal flow in liquid metal blankets and divertors of fusion reactors can be three-dimensional due to the presence of a strong, non-uniform magnetic field [40, 41, 42]. In this section, the study in [41] is considered. In this study, a three-dimensional MHD flow in an insulating circular duct with the fringing magnetic field is investigated. The external magnetic field is applied in the y-direction, i.e. $\mathbf{b} = B_0 B(z)\hat{\mathbf{y}}$, where B_0 is the characteristic magnetic field. Its profile with respect to the flow direction is determined as follows:

$$B(z) = \frac{1}{2}(B_d + B_u) + \frac{1}{2}(B_d - B_u)\tanh(\gamma z) \tag{29}$$

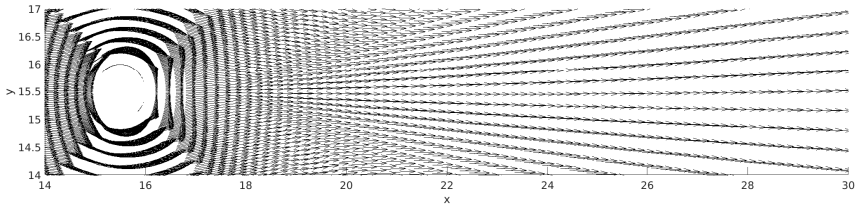
where $B_u = 1$, $B_d = 0.2$ and $\gamma = 0.8$ in this study. The magnetic field is uniform in the upstream region ($B = B_u$ for $z \to -\infty$) and the downstream region ($B = B_d$ for $z \to \infty$) (see Figure 19). In this study, the flow in the duct is considered to be laminar and inertialess. The inertialess flow requires $N >> Ha^{\frac{1}{2}}$, where $Ha = aB_0(\frac{\sigma_f}{\mu_f})^{\frac{1}{2}}$ is the Hartmann number, $N = \frac{a\sigma_f B_0^2}{\mu_f}$ the interaction parameter, B_0 the characteristic magnetic field, a the characteristic length, σ_f the fluid electrical conductivity and μ_f the fluid



(a) $Ha = 1$



(b) $Ha = 5$



(c) $Ha = 10$

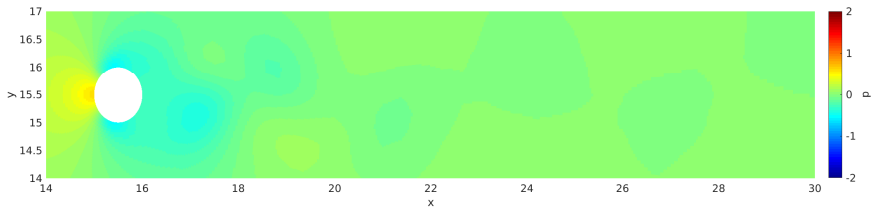
Figure 17: Velocity vector plot for flow over the circle obstacle in the region $(14, 14) \times (30, 17)$

viscosity. The study showed that the three-dimensional MHD effects due to the non-uniform magnetic field can be significant, as the three-dimensional length (d_{3D}) which depends on the three-dimensional pressure drop (Δp_{3D}) was determined to be very high. The three-dimensional pressure drop, Δp_{3D} is defined as follows:

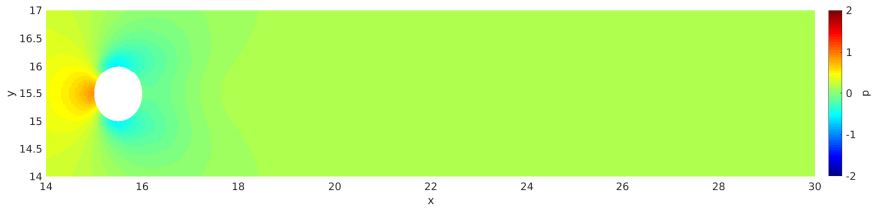
$$\Delta p_{3D} = \Delta p - \frac{3}{16Ha}\pi L(B_u - B_d) \tag{30}$$

where Δp is the pressure drop between $z = -\frac{L}{2}$ and $z = \frac{L}{2}$. The three-dimensional length d_{3D} is then defined as follows:

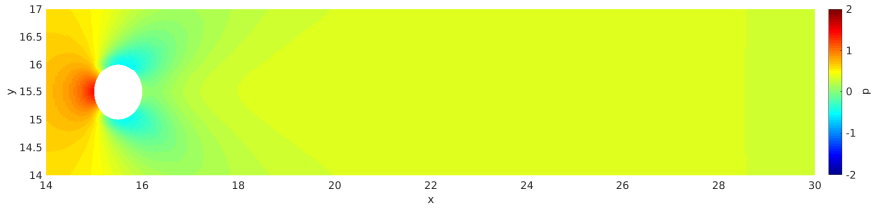
$$d_{3D} = -\frac{\Delta p_{3D}}{dp/dx|_u} = \frac{8Ha}{3\pi}\Delta p_{3D} \tag{31}$$



(a) $Ha = 1$



(b) $Ha = 5$



(c) $Ha = 10$

Figure 18: Pressure distribution for flow over the circle obstacle in the region $(14, 14) \times (30, 17)$

In order to simulate this case, the following three-dimensional computational domain is considered (see Figures 20 and 21). The cross section of the duct is on the (x, y)-plane and this is extended in the z-direction. The computational domain on the (x, z)-plane is shown in Figure 20. The length of the computational domain is set to $L = 100$, while the characteristic length a is the radius of the circular pipe; $a = 1$. In numerical simulations, the computational domain in Figure 21 is extended in the z-direction and is generated via the multiple patch configuration. A graded mesh is employed near the walls. For this example, the DIV-CURL scheme with p_p=1 is employed. For comparison, the Hartmann number Ha=100 is selected. The boundary conditions for the hydrodynamic problem are prescribed as follows: At the inlet (i.e. $z = -\frac{L}{2}$), an inlet velocity, $\mathbf{u}_{in} = (0, 0, u_0)$ is prescribed, where u_0 is the characteristic velocity. At the outlet, the zero Neumann boundary

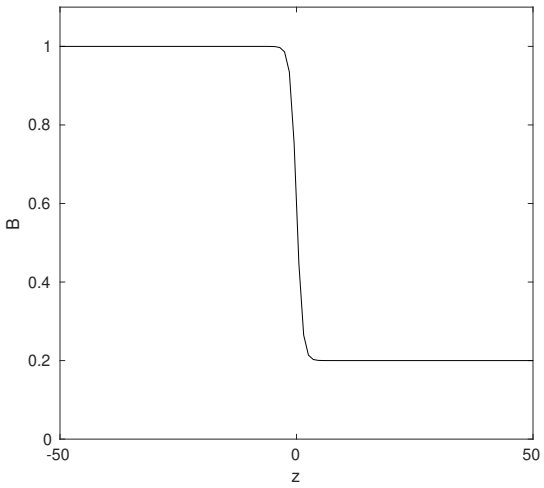


Figure 19: Non-uniform magnetic field with respect to the axial direction

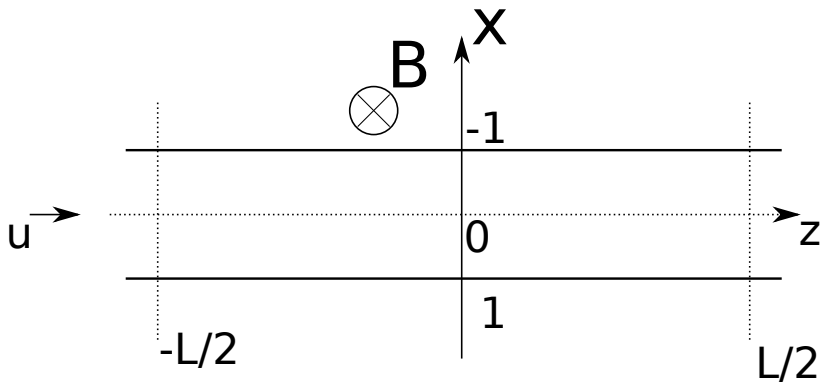


Figure 20: Computational domain on the (x, z)-plane

conditions are applied. No-slip conditions ($\mathbf{u} = 0$) are applied at the walls. For the magnetic problem, the Dirichlet type boundary conditions are applied at the walls, while the Neumann type boundary conditions are applied at the inlet and the outlet. The mesh convergence is carried out to ensure the convergence of the solution. Figure shows the mesh convergence study. It shows that the three-dimensional pressure drop is converged to approximately 3.7E-2 after 2.0E5 unknowns. This value is close to that found in [41], i.e. ∼4.0E-2. Figure 23 shows the axial pressure and core velocity distribution at $x = 0$ and $x = 0.84$. The three-dimensional pressure drop in the

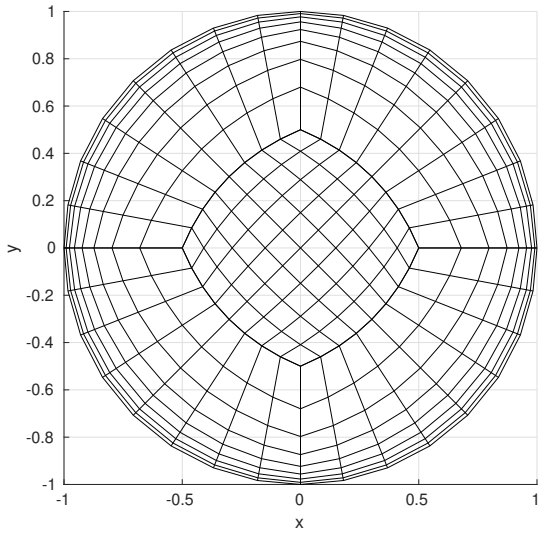


Figure 21: Mesh configuration on the (x, y)-plane

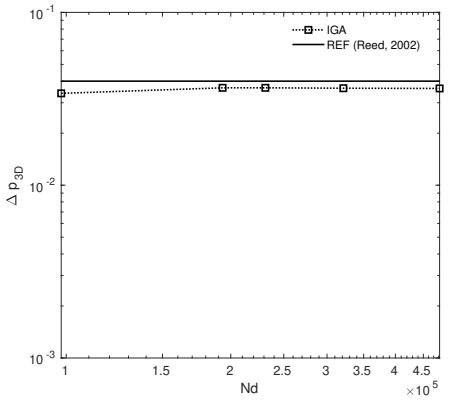
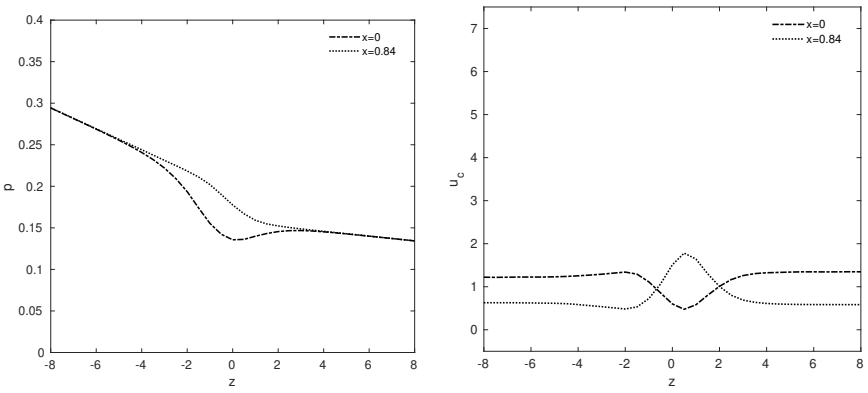


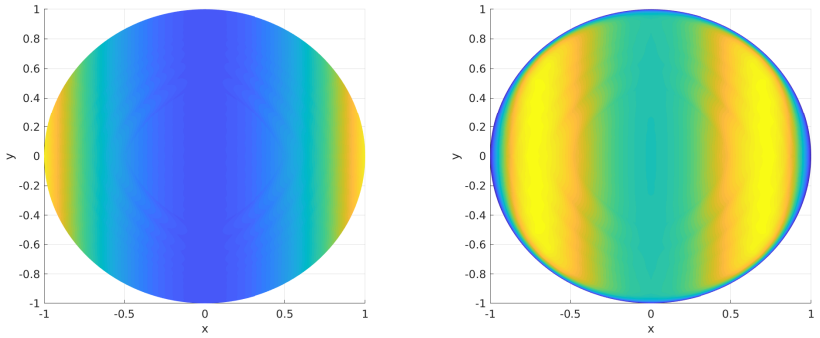
Figure 22: Mesh convergence

region near $z = 0$ is observed due to the change in the magnetic field. The corresponding velocity change in the region $z = 0$ is also observed. Figure 23 shows the distribution of pressure and core velocity on the (x, y)-plane.



(a) Pressure (b) Core velocity

Figure 23: Axial distribution of pressure and core velocity



(a) Pressure (b) Core velocity

Figure 24: Distribution of pressure and core velocity on the (x, y)-plane at $z = 0$

7 Conclusion

In this study, the numerical results of an IGA solver applied to the time-dependent, incompressible MHD equations are presented. Here, two suitable pairs of inf-sup stable discretisations are considered. Convergence studies are carried out to verify and validate the solver using both manufactured and analytical solutions. The problem of flow past an obstacle is also considered. The convergence with respect to the time step size is investigated using a manufactured solution. It is flexible to incorporate both the fully-implicit and semi-implicit time discretisation schemes to the solver presented

in this paper. The differences between the fully-implicit and semi-implicit schemes appear more apparent in the hydrodynamic solutions, whereas they are almost negligible in the magnetic solutions. A dissipative MHD system is considered to examine the energy stability of the proposed solver. This example indicates that the solver may be unconditionally energy stable for all of the spatial and time discretisation schemes considered in this study. Both examples show that for a given time step size, the computational time of the semi-implicit schemes is generally less than the half the computational time of the fully-implicit scheme for the same accuracy. The classic Shercliff problem is then considered to investigate the convergence of the solution with respect to the spatial refinement for both stable discretisations. In this case, it is observed that the accuracy and convergence rates of solution improve as mesh size decreases and polynomial degree increases. It is also shown that the IGA solver generally requires a fewer degrees of freedoms in comparison with the conventional FE. It is concluded that the second-order semi-implicit scheme with DIV-CURL spatial discretisation is the optimal scheme of those studied. However, smooth basis functions from the IGA can lead to higher computational cost, particularly when employing a direct solver. As future work, strategies to optimise the performance of the solver need to be taken into account. In the numerical example, a problem involving the flow past an obstacle is considered. The Strouhal number determined for both the square and circular obstacles at $Ha = 1$ is similar to the results from the available literature. The IGA solver is capable of representing the periodic behaviour of the solution at low Ha and the laminarisation at higher Ha. A benchmark case which studies the effect of non-uniform magnetic field on liquid metal flow in a circular pipe is also considered. The three-dimensional pressure drop and length determined via the simulations agreed well with the available literature. However, there are some limitations to the discretisation schemes considered in this paper. In case of the spatial discresation, it may unnecessarily increase the computational cost, particularly for a large problem due to their tensor-based meshes. This may be improved by implementing some splines which allow a local refinement; for example, T-splines [43], LR B-splines [44] and hierarchical B-splines [45]. Additionally, solving the time-dependent MHD system can be costly due to its coupling between Navier-Stokes and Maxwell's. There are more sophisticated time discretisation schemes that may improve the performance of a solver; e.g. fractional step methods [46], problem-specific preconditioners [47] and projection methods [48]. In order to improve the performance of the solver and to reduce the

computational cost, these may be considered in the future work.

References

[1] A. Christlieb, X. Feng, Y. Jiang, and Q. Tang. A high-order finite difference weno scheme for ideal magnetohydrodynamics on curvilinear meshes. *SIAM Journal on Scientific Computing*, 40(4):A2631–A2666, 2018.

[2] J.N. Shadid, R.P. Pawlowski, J.W. Banks, L. Chacn, P.T. Lin, and R.S. Tuminaro. Towards a scalable fully-implicit fully-coupled resistive mhd formulation with stabilized fe methods. *Journal of Computational Physics*, 229(20):7649 – 7671, 2010.

[3] J.N. Shadid, R.P. Pawlowski, E.C. Cyr, R.S. Tuminaro, L. Chacn, and P.D. Weber. Scalable implicit incompressible resistive mhd with stabilized fe and fully-coupled newtonkrylov-amg. *Computer Methods in Applied Mechanics and Engineering*, 304:1 – 25, 2016.

[4] A. Susanto, L. Ivan, H. De Sterck, and C.P.T. Groth. High-order central eno finite-volume scheme for ideal mhd. *Journal of Computational Physics*, 250:141 – 164, 2013.

[5] J. Ahn and M. Bluck. Isogeometric analysis of the steady-state incompressible mhd equations. *SIAM Journal on Scientific Computing*, 41(2):B396–B424, 2019.

[6] T.J.R. Hughes, J.A. Cottrell, and Y. Bazilevs. Isogeometric analysis: CAD, finite elements, NURBS, exact geometry and mesh refinement. *Computer Methods in Applied Mechanics and Engineering*, 194(39-41):4135 – 4195, 2005.

[7] J.A. Cottrell, A. Reali, Y. Bazilevs, and T.J.R. Hughes. Isogeometric analysis of structural vibrations. *Computer Methods in Applied Mechanics and Engineering*, 195(41–43):5257 – 5296, 2006. John H. Argyris Memorial Issue. Part {II}.

[8] Héctor Gòmez, Victor M. Calo, Yuri Bazilevs, and Thomas J.R. Hughes. Isogeometric analysis of the cahnhilliard phase-field model. *Computer*

Methods in Applied Mechanics and Engineering, 197(49):4333 – 4352, 2008.

[9] Michael J. Borden, Clemens V. Verhoosel, Michael A. Scott, Thomas J.R. Hughes, and Chad M. Landis. A phase-field description of dynamic brittle fracture. *Computer Methods in Applied Mechanics and Engineering*, 217-220:77 – 95, 2012.

[10] JOHN A. EVANS and THOMAS J. R. HUGHES. Isogeometric divergence-conforming b-splines for the steady navierstokes equations. *Mathematical Models and Methods in Applied Sciences*, 23(08):1421–1478, 2013.

[11] John A. Evans and Thomas J.R. Hughes. Isogeometric divergence-conforming b-splines for the unsteady navierstokes equations. *Journal of Computational Physics*, 241:141 – 167, 2013.

[12] Babak S. Hosseini, Matthias M oller, and Stefan Turek. Isogeometric analysis of the Navier - Stokes equations with Taylor - Hood B-spline elements. *Applied Mathematics and Computation*, 267:264 – 281, 2015. The Fourth European Seminar on Computing (ESCO 2014).

[13] A. Buffa, G. Sangalli, and R. Vázquez. Isogeometric analysis in electromagnetics: B-splines approximation. *Computer Methods in Applied Mechanics and Engineering*, 199(17-20):1143 – 1152, 2010.

[14] A. Buffa, J. Rivas, G. Sangalli, and R. Vázquez. Isogeometric discrete differential forms in three dimensions. *SIAM Journal on Numerical Analysis*, 49(2):818–844, 2011.

[15] Prohl, Andreas. Convergent finite element discretizations of the nonstationary incompressible magnetohydrodynamics system. *ESAIM: M2AN*, 42(6):1065–1087, 2008.

[16] Y. He. Unconditional convergence of the Euler semi-implicit scheme for the three-dimensional incompressible MHD equations. *IMA Journal of Numerical Analysis*, 2015.

[17] Y. Zhang, Y. Hou, and L. Shan. Numerical Analysis of the Crank-Nicolson Extrapolation Time Discrete Scheme for Magnetohydrodynamics Flows. *Numerical Methods for Partial Differential Equations*, 2015.

[18] J.A. Cottrell, T.J.R. Hughes, and Y. Bazilevs. *Isogeometric Analysis: Toward Integration of CAD and FEA*. Wiley, 2009.

[19] Peter Monk. *Finite Element Methods for Maxwell's Equations*. Oxford University Press, 2003.

[20] R. Hiptmair. Finite elements in computational electromagnetism. *Acta Numerica*, 2002.

[21] Dominik Schötzau. Mixed finite element methods for stationary incompressible magneto–hydrodynamics. *Numerische Mathematik*, 96(4):771–800, 2004.

[22] J. Ahn. *Isogeometric finite element methods for Liquid Metal Magnetohydrodynamics*. PhD thesis, Imperial College London.

[23] A. Buffa, C. de Falco, and G. Sangalli. Isogeometric analysis: Stable elements for the 2D Stokes equation. *International Journal for Numerical Methods in Fluids*, 65(11-12):1407–1422, 2011.

[24] A. Buffa, G. Sangalli, and R. Vázquez. Isogeometric methods for computational electromagnetics: B-spline and T-spline discretizations. *Journal of Computational Physics*, 257, Part B:1291 – 1320, 2014. Physics-compatible numerical methods.

[25] John A. Evans and Thomas J.R. Hughes. Isogeometric Divergence-conforming B-splines for the Steady Navier-Stokes equations,. Technical report, The Institute for Computational Engineering and Sciences, 2012.

[26] David Silvester, Howard Elman, David Kay, and Andrew Wathen. Efficient preconditioning of the linearized navierstokes equations for incompressible flow. *Journal of Computational and Applied Mathematics*, 128(1):261 – 279, 2001. Numerical Analysis 2000. Vol. VII: Partial Differential Equations.

[27] Michael. Wathen, Chen. Greif, and Dominik. Schtzau. Preconditioners for mixed finite element discretizations of incompressible mhd equations. *SIAM Journal on Scientific Computing*, 39(6):A2993–A3013, 2017.

[28] Michael. Wathen and Chen. Greif. A scalable approximate inverse block preconditioner for an incompressible magnetohydrodynamics model problem. *SIAM Journal on Scientific Computing*, 42(1):B57–B79, 2020.

[29] J. A. Shercliff. Steady motion of conducting fluids in pipes under transverse magnetic fields. *Mathematical Proceedings of the Cambridge Philosophical Society*, 49(1):136–144, 001 1953.

[30] U. Müller and L. Bühler. *Magnetofluiddynamics in Channels and Containers*. Springer Science and Business Media, 2013.

[31] M. Woniak, K. Kunik, M. Paszyski, V.M. Calo, and D. Pardo. Computational cost estimates for parallel shared memory isogeometric multi-frontal solvers. *Computers and Mathematics with Applications*, 67(10):1864 – 1883, 2014.

[32] T. E. Tezduyar and R. Shih. Numerical experiments on downstream boundary of flow past cylinder. *Journal of Engineering Mechanics*, 117(4), 1991.

[33] U. Müller and L. Bühler. *Magnetofluiddynamics in Channels and Containers*. Springer Science and Business Media, 2013.

[34] M. Breuer, J. Bernsdorf, T. Zeiser, and F. Durst. Accurate computations of the laminar flow past a square cylinder based on two different methods: lattice-boltzmann and finite-volume. *International Journal of Heat and Fluid Flow*, 21(2):186 – 196, 2000.

[35] M. Benamour, E. Liberge, C. Bghein, and A. Hamdouni. Numerical simulation of flow around obstacles using lattice boltzmann method. *AIP Conference Proceedings*, 1648(1):850039, 2015.

[36] Hao Zhou, Guiyuan Mo, Feng Wu, Jiapei Zhao, Miao Rui, and Kefa Cen. Gpu implementation of lattice boltzmann method for flows with curved boundaries. *Computer Methods in Applied Mechanics and Engineering*, 225-228:65 – 73, 2012.

[37] C H K Williamson. Vortex dynamics in the cylinder wake. *Annual Review of Fluid Mechanics*, 28(1):477–539, 1996.

[38] Sheng Xu and Z. Jane Wang. An immersed interface method for simulating the interaction of a fluid with moving boundaries. *Journal of Computational Physics*, 216(2):454 – 493, 2006.

[39] F. Armero and J.C. Simo. Long-term dissipativity of time-stepping algorithms for an abstract evolution equation with applications to the incompressible MHD and navier-stokes equations. *Computer Methods in Applied Mechanics and Engineering*, 131(1):41 – 90, 1996.

[40] Chiara Mistrangelo and Leo Bhler. Magnetohydrodynamic flows in liquid metal blankets for fusion reactors. *PAMM*, 17(1):115–118, 2017.

[41] C B Reed. Liquid metal flows in circular insulated ducts in nonuniform magnetic fields. In *Conference: 6th International Symposium on Fusion Nuclear Technology*.

[42] S Molokov and C B Reed. Parametric Study of the Liquid Metal Flow in a Straight Insulated Circular Duct in a Strong Nonuniform Magnetic Field. *Fusion Science and Technology*, 2003.

[43] Y. Bazilevs, V.M. Calo, J.A. Cottrell, J.A. Evans, T.J.R. Hughes, S. Lipton, M.A. Scott, and T.W. Sederberg. Isogeometric analysis using t-splines. *Computer Methods in Applied Mechanics and Engineering*, 199(5):229 – 263, 2010. Computational Geometry and Analysis.

[44] Kjetil Andr Johannessen, Trond Kvamsdal, and Tor Dokken. Isogeometric analysis using lr b-splines. *Computer Methods in Applied Mechanics and Engineering*, 269:471 – 514, 2014.

[45] A.-V. Vuong, C. Giannelli, B. Jttler, and B. Simeon. A hierarchical approach to adaptive local refinement in isogeometric analysis. *Computer Methods in Applied Mechanics and Engineering*, 200(49):3554 – 3567, 2011.

[46] Rong An and Can Zhou. Error analysis of a fractional-step method for magnetohydrodynamics equations. *Journal of Computational and Applied Mathematics*, 313:168 – 184, 2017.

[47] Santiago Badia, Alberto F. Martn, and Ramon Planas. Block recursive LU preconditioners for the thermally coupled incompressible inductionless MHD problem. *Journal of Computational Physics*, 274:562 – 591, 2014.

[48] Rong An and Yuan Li. Error analysis of first-order projection method for time-dependent magnetohydrodynamics equations. *Applied Numerical Mathematics*, 112:167 – 181, 2017.